# Estimating the lateral transfer of organic carbon through the European river network using a land surface model

Haicheng Zhang[1*], Ronny Lauerwald[2], Pierre Regnier[1], Philippe Ciais[3], Kristof Van Oost[4], Victoria Naipal[5], Bertrand Guenet[3], Wenping Yuan[6]

[1]Department Geoscience, Environment & Society-BGEOSYS, Université libre de Bruxelles, 1050 Bruxelles, Belgium

[2] Université Paris-Saclay, INRAE, AgroParisTech, UMR ECOSYS, 78850, Thiverval-Grignon, France

[3]Laboratoire des Sciences du Climat et de l'Environnement, IPSL-LSCE CEA/CNRS/UVSQ, Orme des Merisiers, 91191, Gif sur Yvette, France

[4]UCLouvain, TECLIM - Georges Lemaître Centre for Earth and Climate Research, Louvain-la-Neuve, Belgium

[5]EcoAct/ ATOS, 35 rue de miromesnil, 75008, Paris, France

[6]School of Atmospheric Science, Sun Yat-sen University, Guangzhou, Guangdong, 510275, China

*Correspondence to*: Haicheng Zhang (*haicheng.zhang@ulb.be*)

**Abstract.** Lateral carbon transport from soils to the ocean through rivers has been acknowledged

as a key component of global carbon cycle, but is still neglected in most global land surface

models (LSMs). Fluvial transport of dissolved organic carbon (DOC) and $CO_2$ has been

implemented in the ORCHIDEE LSM, while erosion-induced delivery of sediment and

particulate organic carbon (POC) from land to river was implemented in another version of the

model. Based on these two developments, we take the final step towards the full representation

of biospheric carbon transport through the land-river continuum. The newly developed model,

called ORCHIDEE-$C_{lateral}$, simulates the complete lateral transport of water, sediment, POC,

DOC and $CO_2$ from land to sea through the river network, the deposition of sediment and POC in

the river channel and floodplains, and the decomposition of POC and DOC in transit. We

parameterized and evaluated ORCHIDEE-$C_{lateral}$ using observation data in Europe. The model

explains 94%, 75% and 83% of the spatial variations of observed riverine water discharges,

bankfull water flows and riverine sediment discharges in Europe, respectively. The simulated

long-term average total organic carbon concentrations and DOC concentrations in river flows are

comparable to the observations in major European rivers, although our model generally

overestimates the seasonal variation of riverine organic carbon concentrations. Application of

ORCHIDEE-$C_{lateral}$ for Europe reveals that the lateral carbon transfer affects land carbon

dynamics in multiple ways and omission of this process in LSMs may lead to an overestimation of

4.5% in the simulated annual net terrestrial carbon uptake over Europe. Overall, this study presents a

useful tool for simulating large scale lateral carbon transfer and for predicting the feedbacks

between lateral carbon transfer and future climate and land use changes.

## 1 Introduction

Lateral transfer of organic carbon along the land-river-ocean continuums, involving both spatial redistribution of terrestrial organic carbon and the vertical land-atmosphere carbon exchange, has been acknowledged as a key component of the global carbon cycle (Ciais et al., 2013; Ciais et al., 2021; Drake et al., 2018; Regnier et al., 2013, 2022). Erosion of soils and the associated organic carbon, but also leaching of soil dissolved organic carbon (DOC), represent a non-negligible leak in the terrestrial carbon budget and a substantial source of allochthonous organic carbon to inland waters and oceans (Battin et al., 2009; Cole et al., 2007; Raymond et al., 2013; Regnier et al., 2013). As a result of soil aggregate breakdown and desorption, the accelerated mineralization of these eroded and leached soil carbon loads leads to considerable $CO_2$ emission to the atmosphere (Chappell et al., 2016; Lal, 2003; Van Hemelryck et al., 2011). Meanwhile, the organic carbon that is redeposited and buried in floodplains and lakes might be preserved for a long time, thus creating a $CO_2$ sink (Stallard, 1998; Van Oost et al., 2007; Wang et al., 2010; Hoffmann, 2022). In addition, lateral redistribution of soil material can alter land-atmosphere $CO_2$ fluxes indirectly by affecting soil nutrient availability, terrestrial vegetation productivity and physiochemical properties of inland and coastal waters (Beusen et al., 2005; Vigiak et al., 2017).

Although the important role of lateral carbon transfer in the global carbon cycle has been widely recognized, to date, the estimates of land carbon loss to inland waters, the fate of the terrestrial organic carbon within inland waters, as well as the net effect of lateral carbon transfer on land-atmosphere $CO_2$ fluxes remain largely uncertain (Berhe et al., 2007; Doetterl et al., 2016; Lal, 2003; Stallard, 1998; Wang et al., 2014b; Zhang et al., 2014). Existing estimates of global carbon loss from soils to inland waters vary from 1.1 to 5.1 Pg (=$10^{15}$ g) C per year (yr$^{-1}$) (Cole et al., 2007; Drake et al., 2018), and the estimated net impact of global lateral carbon redistribution on land-atmosphere carbon budget ranges from an uptake of atmospheric $CO_2$ by 1 Pg C yr$^{-1}$ to a land $CO_2$ emission of 1 Pg C yr$^{-1}$ (Lal, 2003; Stallard, 1998; Van Oost et al., 2007; Wang et al., 2017; Regnier et al., 2022). A reliable model which is able to explicitly simulate the lateral carbon flux along the land-river continuum and also the interactions between these lateral fluxes and the comprehensive terrestrial carbon cycle, would thus be necessary for projecting changes in the global carbon cycle more accurately.

65  Global land surface models (LSMs) are important tools to simulate the feedbacks between

66  terrestrial carbon cycle, increasing atmospheric $CO_2$, and climate and land use change. However,

67  the lateral carbon transfer, especially for the particulate organic carbon (POC), is still missing or

68  incompletely represented in existing LSMs (Lauerwald et al., 2017; Lauerwald et al., 2020;

69  Lugato et al., 2016; Naipal et al., 2020; Nakhavali et al., 2021; Tian et al., 2015). It has been

70  hypothesized that the exclusion of lateral carbon transfer in LSMs implies a significant bias in

71  the simulated global land carbon budget (Ciais et al., 2013; Ciais et al., 2021; Janssens et al.,

72  2003). For instance, the study of Nakhavali et al. (2021) suggested that about 15% of the global

73  terrestrial net ecosystem production is exported to inland waters as leached DOC. Lauerwald et

74  al. (2020) showed that the omission of lateral DOC transfer in LSM might lead to significant

75  underestimation (8.6%) of the net uptake of atmospheric carbon in the Amazon basin while

76  terrestrial carbon storage changes in response to the increasing atmospheric $CO_2$ concentrations

77  were overestimated.

78  Over the past decade, a number of LSMs have been developed which represent leaching of DOC

79  from soils (Nakhavali et al. 2018, Kicklighter et al. 2013) or the full transport of DOC through

80  the land-river continuum (Lauerwald et al., 2017; Tian et al., 2015). However, the erosion-

81  induced transport of soil POC, which has also been reported to be able to affect the carbon

82  balance of terrestrial ecosystems strongly (Lal., 2003; Van Oost et al., 2007; Tian et al., 2015), is

83  still not or poorly represented in LSMs. The explicit simulation of the complete transport process

84  of POC at large spatial scales is still a major challenge, due to the complexity of the  processes

85  involved, including  erosion-induced sediment and POC delivery to rivers, deposition of

86  sediment and POC in river channels and floodplains, re-detachment of the previously deposited

87  sediments and POC, decomposition and transformation of POC in riverine and flooding waters,

88  as well as the changes of soil profile caused by erosion and deposition (Doetterl et al., 2016;

89  Naipal et al., 2020; Zhang et al., 2020).

90  Several recent model developments have led to the implementation of the lateral transfer of POC

91  in large-scale LSMs. Despite this, there are still some inevitable limitations in these

92  implementations. The Dynamic Land Ecosystem Model (DLEM v2.0, Tian et al., 2015) is able

93  to simulate the erosion-induced POC loss from soil to river and the transport and decomposition

94  of POC in river networks. However, it does not represent the POC deposition in floodplains, nor

95    the impacts of soil erosion and floodplain deposition on the vertical profiles of soil organic

96    carbon (SOC). The Carbon Erosion DYNAMics model (CE-DYNAM, Naipal et al., 2020)

97    simulates erosion of SOC and its re-deposition on the toe-slope or floodplains, transport of POC

98    along river channels, as well as the impact on SOC dynamics at the eroding and deposition sites.

99    However, running at annual time scale, it mostly addresses the centennial timescale and does not

100   represent deposition and decomposition of POC in river channels. Moreover, CE-DYNAM was

101   only applied over the Rhine catchment and has not been fully coupled into a land surface model,

102   therefore excluding the feedbacks of soil erosion on the fully coupled land and aquatic carbon

103   cycles. There are of course more dedicated hydrology and soil erosion models that explicitly

104   simulate the complete transport, deposition and decomposition processes of POC in small river

105   basins (e.g. Jetten et al., 2003; Nearing et al., 1989; Neitsch et al., 2011). However, it is difficult

106   to apply these models at large spatial scales (e.g. continental or global scale) due to the limited

107   availability of forcing data (e.g. geometric attributes of river channel), suitable model

108   parameterization and computational capacity. Moreover, these models have limited capability of

109   representing the full terrestrial C cycle in response to climate change, increasing atmospheric

110   $CO_2$ and land use change. Therefore, basin-scale models are not an option to assess the impact of

111   soil erosion on the large-scale terrestrial C budget in response to global changes.

112   Here we describe the development, application and evaluation of a new branch of the

113   ORCHIDEE LSM (Krinner et al., 2005), hereafter ORCHIDEE-$C_{lateral}$, that can be used to

114   simulate the complete lateral transfer processes of water, sediment, POC and DOC along the

115   land-river-ocean continuum at large spatial scale (e.g. continental and global scale). In previous

116   studies, the leaching and fluvial transfer of DOC and the erosion-induced delivery of sediment

117   and POC from upland soil to river network have been implemented in two different branches of

118   the ORCHIDEE LSM (i.e. ORCHILEAK (Lauerwald et al., 2017) and ORCHIDEE-MUSLE

119   (Zhang et al., 2020)). For this new branch, we first merged these two branches, and subsequently

120   implemented the fluvial transfer of sediment and POC in the coupled model. ORCHIDEE-$C_{lateral}$

121   is calibrated and evaluated using observation data of runoff, bankfull flow, and riverine loads and

122   concentrations of sediment, POC and DOC across Europe. By applying the calibrated model at

123   European scale, we estimate the magnitude and spatial distribution of the lateral carbon transfer

124   in European catchments during the period 1901-2014, as well as the potential impacts of lateral

125   carbon transfer on the land carbon balance. Comparing simulations results to those of an

126 alternative simulation run with lateral displacement of C deactivated, we finally quantify the

127 biases in simulated land C budgets that arise ignoring the lateral transfers of C along the land-

128 river continuum.

129

130 **2 Model development and evaluation**

131 **2.1 ORCHIDEE land surface model**

132 The ORCHIDEE LSM comprehensively simulates the cycling of energy, water and carbon in

133 terrestrial ecosystems (Krinner et al., 2005). The hydrological processes (e.g. rainfall

134 interception, evapotranspiration and soil water dynamics) and plant photosynthesis in

135 ORCHIDEE are simulated at a time step of 30 minutes. The carbon cycle processes (e.g.

136 maintenance and growth respiration, carbon allocation, litter decomposition, SOC dynamics,

137 plant phenology and mortality) are simulated at daily time step. In its default configuration,

138 ORCHIDEE represents 13 land cover types, with one for bare soil and 12 for lands covered by

139 vegetation (eight types of forests, two types of grasslands, two types of croplands). Given

140 appropriate land cover maps and parametrization, the number of PFTs to be represented can

141 however be adapted (Zhang et al., 2020).

142 Our previous implementations of lateral DOC transfer (Lauerwald et al., 2017) and of POC

143 delivery from upland to river network (Zhang et al., 2020) were both based on the ORCHIDEE

144 branch ORCHIDEE-SOM (Camino-Serrano et al., 2018, Fig. S1), which provides a depth-

145 dependent description of the water and carbon dynamics in soil column. In specific, the vertical

146 soil profile in ORCHIDEE-SOM is described by an 11-layer discretization of a 2 m soil column

147 (Camino-Serrano et al., 2018). Water flows between adjacent soil layers are simulated using the

148 Fokker–Planck equation that resolves water diffusion in non-saturated conditions (Campoy et al.,

149 2013; Guimberteau et al., 2018). Free gravitational drainage occurs in the lowest soil layer when

150 actual soil water content is higher than the residual water content (Campoy et al., 2013).

151 Following the CENTURY model (Parton et al., 1988), ORCHIDEE-SOM represents two litter

152 pools (metabolic and structural) and three SOC pools (active, slow and passive) that differ in

153 their respective turnover times. The decomposition of each carbon pool is calculated by first

154 order kinetics based on the corresponding turnover time, soil moisture and temperature as

155 controlling factors, as well as the priming effects of fresh organic matter (Guenet et al., 2018;

156 Guenet et al., 2016). Soil DOC is represented by a labile and a refractory DOC pools, with a high

157 and low turnover rate, respectively. Each DOC pool may be in the soil solution or adsorbed on

158 the mineral matrix. The products of litter and SOC decomposition enter the free DOC pool,

159 which in turn is decomposed following first order kinetics (Kalbitz et al., 2003) and returns back

160 to SOC. Adsorption and desorption of DOC follows an equilibrium distribution coefficient

161 calculated from soil clay and pH. Free DOC can be transported with the water flux simulated by

162 the soil hydrological module of ORCHIDEE. However, DOC adsorbed to soil minerals can

163 neither be decomposed nor transported (Camino-Serrano et al., 2018). All the described

164 processes occur within each soil layer. At each time step, "the flux of DOC leaving the soil is

165 calculated by multiplying DOC concentrations in soil solution with the runoff (surface layer) and

166 drainage (bottom layer) flux simulated by the hydrological module" (Camino-Serrano et al.,

167 2018, p. 939). More detailed information about the simulation of soil hydrological and

168 biogeochemical processes in ORCHIDEE-SOM can be found in Guenet et al. (2016) and

169 Camino-Serrano et al. (2018).

170 **2.1.1 Lateral transfer of DOC and $CO_2$**

171 Lateral transfer of DOC and dissolved $CO_2$ from land to ocean through river network has been

172 implemented in the ORCHILEAK (Lauerwald et al., 2017), an ORCHIDEE branch developed

173 from ORCHIDEE-SOM (Fig. S1). The method used in ORCHILEAK to simulate the adsorption,

174 desorption, production, consumption and transport of DOC within the soil column, as well as

175 DOC export from the soil column with surface runoff and drainage is similar to that used in

176 ORCHIDEE-SOM. Besides the decomposition of SOC and litter, ORCHILEAK also represents

177 the contribution of wet and dry deposition to soil DOC via throughfall. The direct DOC input

178 from rainfall to aquatic DOC pools is simulated based on the DOC concentration in rainfall and

179 the area fraction of stream and flooding waters in each basin (Table 1). Note that the maximum

180 area fractions of river surface and floodplain in each basin (i.e. each 0.5°×0.5° grid cell in this

181 study) are derived from high-resolution topographic data (Table 1). As it is difficult to explicitly

182 represent all real river channels in a global land surface model (due to the limit of computing

183 efficiency of current computers), we assume that there is one virtual river channel in each

184     $0.5° \times 0.5°$ pixel. The surface area of this virtual river is the sum of all real rivers and the flow

185     direction of this virtual is assumed to be same to the largest real river (Lauerwald et al., 2015).

186     Simulation of the lateral transfer of DOC and $CO_2$ in river networks, i.e. the transfer of DOC and

187     $CO_2$ from one basin to another based on the stream flow directions obtained from a forcing file

188     ($0.5°$, Table 1), follows the routing scheme of water (Guimberteau et al., 2012). For each basin

189     with floodplain (defined by forcing data), bankfull flow occurs when stream volume in the river

190     channel exceeds a threshold prescribed by the forcing file (Table 1). DOC and $CO_2$ in flooding

191     waters can enter into soil DOC and $CO_2$ pools along with the flooding water infiltrated into soil.

192     The infiltration rate of flooding water depends on soil properties and soil water content, but does

193     not depend on vegetation cover. On the contrary, DOC and $CO_2$ originated from the

194     decomposition of submerged litter and SOC in the floodplains are added to the overlying

195     flooding waters. Note that the turnover times of litter and SOC under flooding waters are

196     assumed to be three times of the litter and SOC turnover times in upland soil (Reddy & Patrick

197     Jr, 1975; Neckles & Neill, 1994; Lauerwald et al., 2017). After removing the infiltrated and

198     evaporated water, the amount of the remaining flooding water, as well as the DOC and dissolved

199     $CO_2$ returning to river channel at the end of each day is calculated based on a time constant of

200     flooding water (= 4.0 days, d'Orgeval et al., 2008) modified by a basin-specific topographic

201     index ($f_{topo}$, unitless) (Lauerwald et al., 2017).

202

203     **Table 1.** List of forcing data needed to run ORCHIDEE-$C_{lateral}$ and the data used to evaluate the

204     simulation results. $S_{res}$ and $T_{res}$ are the spatial and temporal resolution of the forcing data,

205     respectively.

| | Data | $S_{res}$ | $T_{res}$ | Data source |
|---|---|---|---|---|
| Forcing | Climatic forcing data (precipitation, temperature, incoming shortwave/longwave radiation, air pressure, wind speed, relative humidity) | 0.5° | 3 hour | GSWP3 database (Dirmeyerm et al., 2006) |
| | Land cover | 0.5° | 1 year | LUHa.rc2 database (Chini et al., 2014) |
| | Soil texture class | 0.5° | – | Reynolds et al. (1999) |

| | | | |
|---|---|---|---|
| Soil bulk density and pH | 30″ | – | HWSD v1.2 (FAO/IIASA/ISRIC/ISSCAS/JRC, 2012) |
| Stream flow directions, topographic index ($f_{topo}$) | 0.5° | – | STN-30p (Vörösmarty et al., 2000) |
| Area fraction of floodplains | 250 m | – | GFPLAIN250m (Nardi et al., 2019)[a] |
| Area fraction of river surface | 0.5° | – | Lauerwald et al. (2015) |
| Maximum water storage in river channel ($S_{rivmax}$) | 0.5° | – | Derived from pre-runs with ORCHIDEE-C$_{lateral}$ (see section 2.3) |
| Reference sediment delivery rate ($SED_{ref}$) | 0.5° | – | Zhang et al. (2020) |
| Digital Elevation Model (DEM) | 3″ | – | HydroSHEDS (Lehner et al., 2008) and GDEM v3 (Abrams et al., 2020) [b] |
| **Validation** Riverine water discharge | – | 1 day | GRDC[c] |
| Bankfull flow | – | 1 year | Schneider et al. (2011) |
| Sediment delivery from upland to inland waters | 100 m | 1 year | Borrelli et al. (2018) |
| Riverine sediment discharge | – | 1 year | European Environment Agency[d] and publications[e] |
| Riverine POC and DOC concentration | – | Instantaneous | GLORICH (Hartmann et al., 2019) |
| | 30″ | | HWSD v1.2 |
| | 5′ | | GSDE (Shangguan et al., 2014) |
| SOC stock | 250 m | – | SoilGrids (Hengl et al., 2014) |
| | 10 km | | S2017 (Sanderman et al., 2017) |
| | 250 m | | LandGIS[f] |

[a] The GFPLAIN250m only covers the regions south of 60° N. We produced map of floodplain distribution in regions north of the 60° N using the same method for producing GFPLAIN250m (Nardi et al., 2019) based on the ASTER GDEM v3 database (Abrams et al., 2020). [b] The DEM data from HydroSHEDS and GDEM v3 are used to extract the topographic properties (e.g. location, area and average slope) of headwater basins in regions south and north of 60° N, respectively. [c] The Global Runoff Data Centre, 56068 Koblenz, Germany. [d] https://www.eea.europa.eu/data-and-maps/data/sediment-discharges. [e] Publications including Van Dijk & Kwaad, 1998; Vollmer & Goelz, (2006) and Reports of the DanubeSediment project (Sediment Management Measures for the Danube, http://www.interreg-danube.eu/approved-projects/danubesediment). [f] https://zenodo.org/record/2536040#.YC-QGo9KiUm.

216     Decomposition of DOC in stream and flooding waters is calculated at daily time step based on

217     the prescribed turnover times of labile (2 days) and refractory (80 days) DOC in waters (when

218     temperature is 28 °C) and a temperature factor obtained from Hanson et al. (2011). $CO_2$ evasion

219     in inland waters is simulated using a much finer integration time step of 6 minutes. The $CO_2$

220     partial pressures ($pCO_2$) in water column is first calculated based on the temperature-dependent

221     solubility of $CO_2$ and the concentration of dissolved $CO_2$ (Telmer and Veizer, 1999). Then the

222     $CO_2$ evasion is calculated based on the gas exchange velocity, the water–air gradient in $pCO_2$,

223     and the surface water area available for gas exchange (Lauerwald et al., 2017). The effect of

224     wind speed on $CO_2$ evasion is not represented in the current version of ORCHILEAK. In

225     addition, swamp and wetland are represented in the routing scheme of ORCHILEAK. More

226     detailed descriptions can be found in Lauerwald et al. (2017).

**2.1.2 Sediment and particulate organic carbon delivery from upland soil to river network**

228     To give an accurate simulation of sediment delivery from uplands to river network and maintain

229     computational efficiency, an upscaling scheme which integrates information from high-resolution (3″)

230     topographic and soil erodibility data into a LSM forcing file at 0.5° spatial resolution, has been introduced

231     (see details in Zhang et al., 2020, Fig. 1). With this upscaling scheme, the erosion-induced sediment and

232     POC delivery from upland soils to the river network, as well as the changes in SOC profiles due to soil

233     erosion had already been implemented in ORCHIDEE-MUSLE (Zhang et al., 2020). The sediment

234     delivery from small headwater basins (which are basins without perennial stream and are extracted from

235     high-resolution (e.g. 3″) digital elevation model (DEM) data, Figs. 1a&d) to the river network (i.e. gross

236     upland soil erosion – sediment deposition within headwater basins) is simulated using the Modified

237     Universal Soil Loss Equation model (MUSLE, Williams, 1975). As introduced in Zhang et al. (2020),

238     "the daily sediment delivery rate from each headwater basin ($S_{i\_ref}$, Mg day$^{-1}$ basin$^{-1}$) is first calculated for

239     a given set of reference runoff and vegetation cover conditions (Fig. 1e):

$$S_{i\_ref} = a\left(Q_{i\_ref}\, q_{i\_ref}\right)^{b} K_i LS_i C_{ref} P_{ref} \tag{1}$$

241     where $Q_{i\_ref}$ is the total water discharge (m$^3$ day$^{-1}$) at the outlet of headwater basin $i$ for the daily

242     reference runoff condition ($R_{ref}$) of 10 mm day$^{-1}$ (*see* Table S1 for the definitions of all

243     abbreviations used in this study). In Eq. 1, $q_{i\_ref}$ is the daily peak flow rate (m$^3$ s$^{-1}$) at the

244     headwater basin outlet under the assumed reference runoff condition. Similar to the SWAT

245     model (Soil and Water Assessment Tool, Neitsch et al., 2011), $q_{i\_ref}$ was calculated from the

246 reference maximum 30-minutes runoff (= 1 mm 30-minutes⁻¹) depth and drainage area ($DA_i$, m²)

247 according to the following equation:

$$q_{i\_ref} = \frac{R_{30\_ref}}{30 \times 60} \left( DA_i^{(d\,DA_i^c)} \right) 1000 \tag{2}$$

249 where $R_{30\_ref}$ (= 1 mm 30-minutes⁻¹) is the assumed daily maximum 30-minutes runoff". The

250 coefficients $a$ and $b$ in Eq. 1 and $c$ and $d$ in Eq. 2 need to be calibrated (see section 2.3 and Table

251 2). In Eq. 1, the term $LS_i$ is the combined dimensionless slope length and steepness factor

252 calculated based on the $DA_i$ and the average slope steepness (extracted from DEM) of headwater

253 basin $i$ (Moore and Wilson, 1992). $C_{ref}$ (0-1, dimensionless) in Eq. 1 represents the cover

254 management factor which depends on vegetation cover and storage of plant debris (see below).

255 The value of $C_{ref}$ is set to 0.1 for the reference state. The soil erodibility factor $K_i$ (Mg MJ⁻¹ mm⁻

256 ¹) is calculated using the method of the EPIC model (Sharpley and Williams, 1990) based on

257 SOC and soil texture data obtained from the GSDE database (Table 1). The term $P_{ref}$ (0-1,

258 dimensionless) in Eq. 1 is a factor representing erosion control practices. It was set to 1, as we

259 did not consider the impacts of soil conservation practices in reducing soil erosion rate. Note that

260 it does not matter which value is chosen for the $R_{ref}$, $R_{30\_ref}$ and $C_{ref}$ as long as they are used

261 consistently throughout a study.
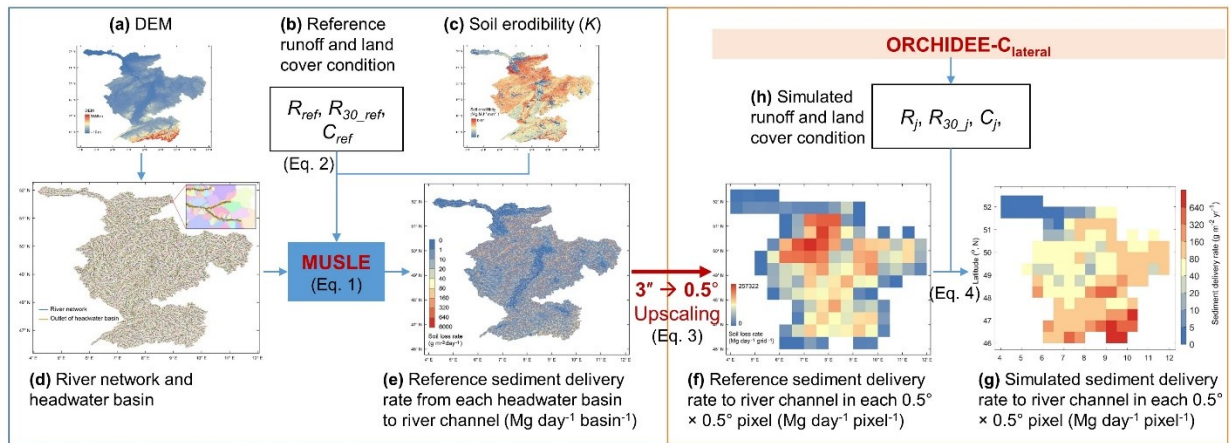
262

263 **Figure 1** Upscaling scheme used in ORCHIDEE-MUSLE (Zhang et al., 2020) and ORCHIDEE-

264 C_lateral for calculating the sediment delivery rate from headwater basins to river networks.

265 MUSLE is the Modified Universal Soil Loss Equation; DEM is the digital elevation model (m);

266 $K$ is the soil erodibility factor (Mg MJ-1 mm-1); $R_{ref}$ is the assumed reference daily runoff depth

267 (= 10 mm day⁻¹); $R_{30\_ref}$ is the assumed reference maximum 30-minutes runoff depth (= 1 mm

268    30-minutes$^{-1}$); $C_{ref}$ (= 0.1, dimensionless) is the assumed reference cover management factor;

269    $R_{iday}$, $R_{30\_iday}$ and $C_{iday}$ are the simulated daily total runoff depth, daily maximum 30-minutes

270    runoff depth and daily cover management factor, respectively. This figure is adapted from the

271    Fig. 1 in Zhang et al. (2020).

272

273    For the use of these reference sediment delivery estimates in ORCHIDEE-C$_{lateral}$, the values were

274    first calculated for each headwater basin derived from high resolution geodata (Fig. 1e), then

275    aggregated to 0.5° grid cells (Fig. 1f) – the scale used in our simulations and required to maintain

276    computational efficiency (also limited by the availability of climate and land cover forcing data).

277    This aggregated dataset is then used to force the simulation of the actual daily sediment delivery

278    ($S_j$, g day$^{-1}$ grid$^{-1}$) in ORCHIDEE-C$_{lateral}$, simply based on the estimated reference sediment

279    delivery rates of Eq. (1) and on the ratios between actual runoff and land cover conditions and

280    the assumed reference conditions used to create that forcing file (Eq. 4, Fig. 1g).

281    $$S_{ref} = \sum_{i=1}^{n}\left(S_{i\_ref}\right) \times 10^6 \tag{3}$$

282    $$S_j = S_{ref}\left(\frac{R_j \, R_{30\_j}}{R_{ref} \, R_{30\_ref}}\right)^b \frac{C_j}{C_{ref}} \tag{4}$$

283    where $R_j$ (mm day$^{-1}$) is the total surface runoff on day $j$ simulated by the hydrological module or

284    ORCHIDEE-MUSLE at 0.5° spatial resolution every 30 minutes. $R_{30\_j}$ (mm 30-min$^{-1}$) is the

285    maximum value of the 48 half-hour runoffs in each day. $C_j$ (0-1, unitless) is the daily actual

286    cover management factor, calculated based on the fraction of surface vegetation cover, the

287    amount of litter stock and the biomass of living roots in each PFT within each 0.5°×0.5° grid

288    cell. $R_{ref}$, $R_{30\_ref}$, $C_{ref}$ and $P_{ref}$ are the reference values used to estimate the reference sediment

289    delivery rates as describe above.

290    Daily POC delivery to river headstream in each 0.5° grid cell is finally simulated based on the

291    sediment delivery rate and the average SOC concentration of surface soil layers (0-20 cm). We

292    assumed that litter cannot be eroded and transported to the river network, however, it can affect

293    soil erosion rate through the cover management factor of the MUSLE model (denoted by $C_j$, Eq.

294    4). The vertical SOC profile is updated every day based on the average depth of eroded soil for

295    each PFT in each 0.5° grid cell of ORCHIDEE. For more detailed description of the

296    ORCHIDEE-MUSLE, we refer to Zhang et al. (2020).

297

## 2.2 Sediment and POC transport in inland water network

299    Through the merge of the model branches ORCHILEAK and ORCHIDEE-MUSLE, the new

300    branch ORCHIDEE-C$_{lateral}$ combines the novel features of both sources (DOC and POC)

301    described above. The development of ORCHIDEE-C$_{lateral}$ is complemented by a representation of

302    the sediment and POC transport through the river network that is completely novel and described

303    below.

### 2.2.1 Sediment transport

305
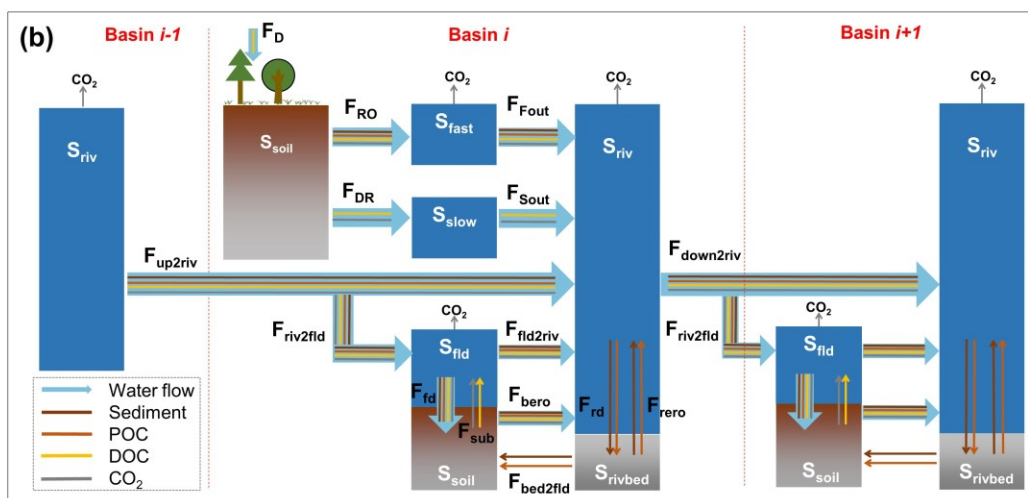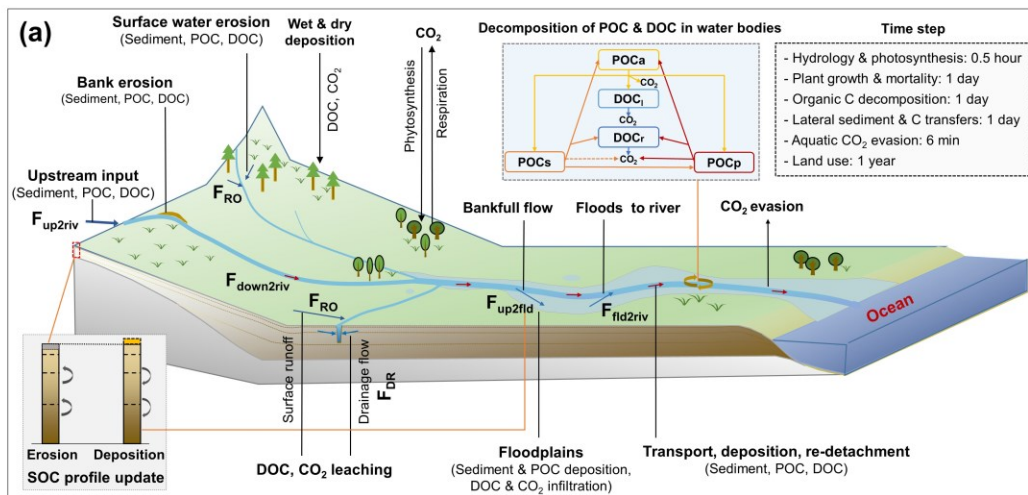
**Figure 2** Simulated lateral transfer processes of water, sediment and carbon (POC, DOC and $CO_2$) in ORCHIDEE-$C_{lateral}$ (a) and a schematic plot for the reservoirs and flows of water, sediment and carbon represented in the routing module of ORCHIDEE-$C_{lateral}$ (b). $S_{soil}$ is the soil pool. $S_{rivbed}$ is the sediment (also POC) deposited on the river bed. $S_{fast}$, $S_{slow}$, $S_{riv}$ and $S_{fld}$ are the 'fast', 'slow', stream and flooding water reservoir, respectively. $F_{RO}$ and $F_{DR}$ are the surface runoff and belowground drainage, respectively. $F_{Fout}$ and $F_{Sout}$ are the flows from fast and slow reservoir to the stream reservoir, respectively. $F_{up2riv}$ and $F_{down2riv}$ are the upstream inputs and downstream outputs, respectively. $F_{riv2fld}$ is the outputs from river stream to the flooding reservoir. $F_{fld2riv}$ is the return flow from flooding reservoir to stream reservoir. $F_{bed2fld}$ is the transform from deposited sediment in river bed to floodplain soil. $F_{bero}$ is bank erosion. $F_{rd}$ and $F_{rero}$ are the deposition and re-detachment of sediment and POC in river channel, respectively. $F_{sub}$ is the flux of DOC and $CO_2$ from floodplain soil (originated from the decomposition of submerged litter and soil carbon) to the overlying flooding water. $F_{fld}$ is the deposition of sediment and POC and the infiltration of water and DOC. $F_D$ is the wet and dry deposition of DOC from atmosphere and plant canopy. $DOC_l$ and $DOC_r$ are the labile and refractory DOC pool, respectively. $POC_a$, $POC_s$ and $POC_p$ are the active, slow and passive POC pool, respectively.

Simulation of sediment transport through the river network basically follows the routing scheme of surface water and DOC of ORCHILEAK (Fig. 2). Along with surface runoff ($F_{RO\_h2o}$, $m^3$ $day^{-1}$), the sediment delivery ($F_{RO\_sed}$, g $day^{-1}$) from uplands in each basin (i.e. each 0.5° grid cell in the case of this study) initially feeds an aboveground water reservoir ($S_{fast\_h2o}$, $m^3$) with a so-called fast water residence time. From this fast water reservoir, a delayed outflow feeds into the so-called stream reservoir ($S_{riv}$, $m^3$, Fig. 2b). Daily water ($F_{Fout\_h2o}$, $m^3$ $day^{-1}$) and sediment ($F_{Fout\_sed}$, g $day^{-1}$) flows from fast water reservoir to stream reservoir are calculated from a grid cell-specific topographic index $f_{topo}$ (unitless, Vörösmarty et al., 2000) extracted from a forcing file (Table 1) and a reservoir-specific factor $\tau$ which translates $f_{topo}$ into a water residence time of each reservoir (Eqs. 5, 6). Following Guimberteau et al. (2012), the $\tau$ of the fast water reservoir ($\tau_{fast}$) is set to 3.0 days. As the sediment delivery calculated from MUSLE is the net soil loss from headwater basins (gross soil erosion – soil deposition within headwater basins), we assumed that there is no sediment deposition in the fast reservoir, and that all of the sediment in the fast reservoir enters the stream reservoir. In addition, only the surface runoff causes soil

337     erosion. The belowground drainage ($F_{DR\_h2o}$, $m^3$ $day^{-1}$) only transports DOC and dissolved $CO_2$

338     to the stream reservoir (Fig. 2b).

$$F_{Fout\_h2o} = \frac{S_{fast\_h2o}}{\tau_{fast} f_{topo}} \tag{5}$$

$$F_{Fout\_sed} = \frac{S_{fast\_sed}}{\tau_{fast} f_{topo}} \tag{6}$$

341     The budget of the suspended sediment in the stream ($S_{riv\_sed}$, g) is determined by $F_{out\_sed}$, the

342     upstream sediment input ($F_{up2riv\_sed}$, g $day^{-1}$), the sediment input by flooding water returning to

343     the river ($F_{fld2riv\_sed}$, g $day^{-1}$), the re-detachment of the previously deposited sediment in the river

344     bed ($F_{rero\_sed}$, g $day^{-1}$), the bank erosion ($F_{bero\_sed}$, g $day^{-1}$), the sediment deposition in the river

345     bed ($F_{rd\_sed}$, g $day^{-1}$) and the sediment transported to downstream river stretches ($F_{down2riv\_sed}$, g

346     $day^{-1}$) and, occasionally, floodplains ($F_{riv2fld\_sed}$, g $day^{-1}$) (Eq. 7).

$$\frac{dS_{riv\_sed}}{dt} = F_{Fout\_sed} + F_{up2riv\_sed} + F_{fld2riv\_sed} + F_{rero\_sed} + F_{bero\_sed} - F_{rd\_sed} - F_{down2riv\_sed} - F_{riv2fld\_sed} \tag{7}$$

348     Sediment transport capacity (TC, g m-3) is defined as the maximum concentration of suspended

349     sediment that a given flow rate can carry. TC and the flow rate determine the amount of sediment

350     that can be transported to the downstream grid cell (e.g. $F_{down2riv\_sed}$, $F_{riv2fld\_sed}$). Suspended

351     sediment loads that are in excess to maximum possible amount of transported sediment will

352     deposit on the river bed ($F_{rd\_sed}$). If sediment loads are below that maximum possible amount,

353     erosion of the river bed ($F_{rero\_sed}$) or river bank ($F_{bero\_sed}$) takes place (Arnold et al., 1995;

354     Nearing et al., 1989; Neitsch et al., 2011).

355     In this study, we used an empirical equation adapted from the WBMsed model, which has been

356     proven effective in simulating the suspended sediment discharges in global large rivers (Cohen et

357     al., 2014), to estimate the *TC* of suspended sediment concentration in stream flow (g $m^{-3}$):

$$TC = \frac{\omega \, q_{ave}^{0.3} \, A^{0.5} \left(\frac{q_{iday}}{q_{ave}}\right)^{e_1} (24 \times 60 \times 60)}{F_{down2riv\_h20}} \tag{8}$$

$$e_1 = 1.5 - max(0.8, 0.145 \log_{10} DA) \tag{9}$$

360     where $\omega$ is the coefficient of proportionality, $q_{ave}$ ($m^3$ $s^{-1}$) is long-term average stream flow rate

361     obtained from an historical simulation by ORCHILEAK (Table 1), $q_j$ ($m^3$ $s^{-1}$) is stream flow rate

362     on day $j$, $e_1$ is an exponent depending on the upstream drainage area ($DA$, $m^2$), $F_{down2riv\_h20}$ ($m^3$

day$^{-1}$) is the daily downstream water discharge from the stream reservoir. In the stream reservoir of each basin, net deposition occurs when $TC$ is smaller than the concentration of suspended sediment, and the daily deposited sediment ($F_{rd\_sed}$, g day$^{-1}$) is calculated based on the surplus of the suspended sediment:

$$F_{rd\_sed} = c_{rivdep}\left(S_{riv\_sed} - TC\, S_{riv\_h2o}\right) \tag{10}$$

where $c_{rivdep}$ (0-1, unitless) is the daily deposited fraction of the sediment surplus. Net erosion of the previously deposited sediment in river bed ($S_{rivbed\_sed}$, Fig. 2) or the river bank occurs when $TC$ is larger than the concentration of suspended sediment. We assumed that the erosion of river bank occurs only after all of the $S_{rivbed\_sed}$ has been eroded. Thus the daily erosion rate ($F_{rero\_sed}$, g day$^{-1}$) in river channel is calculated as:

$$F_{rero\_sed} = \begin{cases} c_{ebed}\left(TC\, S_{riv\_h2o} - S_{riv\_sed}\right), & c_{ebed}\left(TC\, S_{riv\_h2o} - S_{riv\_sed}\right) \le S_{rivbed\_sed} \\ S_{rivbed\_sed} + c_{ebank}\left(TC\, S_{riv\_h2o} - S_{riv\_sed} - S_{rivbed\_sed}\right), & c_{ebed}\left(TC\, S_{riv\_h2o} - S_{riv\_sed}\right) > S_{rivbed\_sed} \end{cases} \tag{11}$$

where $c_{ebed}$ (0-1, unitless) and $c_{ebank}$ (0-1, unitless) are the fraction of sediment deficit that can be complemented by erosion of river bed and bank, respectively. After updating the $S_{riv\_sed}$ based on the $F_{rd\_sed}$ or $F_{rero\_sed}$, the sediment discharge to downstream basin ($F_{down2riv\_sed}$, g day$^{-1}$) is calculated based on the ratio of downstream water discharge to the total stream reservoir:

$$F_{down2riv\_sed} = \left(S_{riv\_sed} - F_{rd\_sed} + F_{rero\_sed}\right)\frac{F_{down2riv\_h2o}}{S_{riv\_sh2o}} \tag{12}$$

In each basin, the bankfull flow occurs when $S_{riv\_h2o}$ exceeds the maximum water storage of river channel ($S_{rivmax}$, g), which is defined by a forcing file (Table 1). Sediment flow from stream to floodplain ($F_{riv2fld\_sed}$, g day$^{-1}$) follows the flooding water, and it is calculated as:

$$F_{riv2fld\_sed} = \left(S_{riv\_sed} - F_{rd\_sed} + F_{rero\_sed}\right)\frac{F_{riv2fld\_h2o}}{S_{riv\_sh2o}} \tag{13}$$

$$F_{riv2fld\_h2o} = \left(S_{riv\_h2o} - F_{down2riv\_h2o} - S_{rivmax}\right)\frac{f_{A\_fld}}{f_{A\_fld} + f_{A\_riv}} \tag{14}$$

where $f_{A\_fld}$ (0-1, unitless) and $f_{A\_riv}$ (0-1, unitless) is the fraction of floodplain area and river surface area in each basin, respectively. Following the routing scheme of ORCHILEAK, the bankfull flow of a specific basin is assumed to enter the floodplain in the neighbouring downstream basin instead of the basin where it originates.

388  The sediment balance in flooding reservoir ($S_{fld\_sed}$, g) is controlled by sediment input from the

389  upstream basins ($F_{riv2fld\_sed}$, g day⁻¹), the sediment flowing back to the stream reservoir ($F_{fld2riv\_sed}$,

390  g day⁻¹) and the sediment deposition ($F_{fd\_sed}$, g day⁻¹) (Fig. 2):

391  $$\frac{dS_{fld\_sed}}{dt} = F_{riv2fld\_sed} - F_{fld2riv\_sed} - F_{fd\_sed} \qquad (15)$$

392  Sediment deposition in floodplain is calculated as the sum of a natural deposition and the

393  deposition due to evaporation ($E_{h2o}$, m³ day⁻¹) and infiltration ($I_{h2o}$, m³ day⁻¹) of the flooding

394  waters:

395  $$F_{fd\_sed} = c_{flddep}\, S_{fld\_sed} + S_{fld\_sed} \frac{E_{h2o} + I_{h2o}}{S_{fld\_h2o}} \qquad (16)$$

396  where $c_{flddep}$ (0-1, unitless) is the daily deposited fraction of the suspended sediment in flooding

397  waters. After removing the deposited sediment from $S_{fld\_sed}$, $F_{fld2riv\_sed}$ is calculated based on the

398  ratio of ratio of $F_{fld2riv\_h2o}$ to the total flooding reservoir:

399  $$F_{fld2riv\_sed} = S_{fld\_sed} \frac{F_{fld2riv\_h2o}}{S_{fld\_h2o} - E_{h2o} - I_{h2o}} \qquad (17)$$

400

401  $$F_{fld2riv\_h2o} = \frac{S_{fld\_h2o} - E_{h2o} - I_{h2o}}{\tau_{flood}\, f_{topo}} \qquad (18)$$

402  where $\tau_{flood}$ is a factor which translates $f_{topo}$ (Table 1) into a water residence time of the flooding

403  reservoir. Same to ORCHILEAK, it is set to 1.4 (day m⁻²) in this study.

404  Note that as the upland soil in ORCHIDEE is composed of clay, silt and sand particles, so that

405  the dynamics of clay-, silt- and sand-sediment in inland waters are simulated separately. To

406  represent the selective transport of clay-, silt- and sand-sediment, the model parameter $\omega$ (Eq. 8)

407  and $c_{rivdep}$ (Eq. 10) are set to different values when calculating the sediment transport capacity

408  and the deposition of surplus suspended sediment for different particle sizes (Table 2).

409  Moreover, as our model mainly aims to simulate the lateral transfer of sediment and carbon at

410  the decadal to centennial timescale, rather than covering the past thousands of years or even

411  longer time periods, we did not consider the evolution and diversion of river channels in our

412  study.

### 2.2.2 POC transport and decomposition

Many studies described the selective transport of POC and sediment of different particle sizes. The enrichment ratio (defined as the ratios of fraction of any given component in the transported sediment to that in the eroded soils) of POC in the transported sediment generally showed significant positive correlation to the fine sediment particles (e.g. fine silt and clay), but negative correlation to the coarse sediment particles (Galy et al., 2008; Haregeweyn et al., 2008; Nadeu et al., 2011; Nie et al., 2015). In ORCHIDEE-C$_{lateral}$, the physical movements of POC in inland water systems are simply assumed to follow the flows of finest clay-sediment (Fig. 2b). For example, the fractions of riverine suspended POC which is deposited on the river bed ($F_{rd\_POC}$, g C day$^{-1}$) or is transported to the river channel ($F_{down2riv\_POC}$, g C day$^{-1}$) or floodplain ($F_{riv2fld\_POC}$, g C day$^{-1}$) are assumed to be equal to the corresponding fractions of clay-sediment (Eqs. 19-21). Also flows of suspended POC in flooding waters to floodplain soil ($F_{fd\_POC}$, g C day$^{-1}$) or back to the stream reservoir ($F_{fld2riv\_POC}$, g C day$^{-1}$), as well as the resuspension of POC from the river bed ($F_{rero\_POC}$, g C day$^{-1}$) are scaled to the simulated flows of clay-sediment (Eqs. 22-24). Note that, similar to SOC, the POC in aquatic reservoirs are divided into three pools: the active ($POC_a$), slow ($POC_s$) and passive pool ($POC_p$) (Fig. 2a). The eroded active, slow and passive SOC flow into the corresponding POC pools in the 'fast' water reservoir (Fig. 2b).

$$F_{rd\_POC} = S_{riv\_POC} \frac{F_{rd\_sed\_clay}}{S_{riv\_sed\_clay}} \tag{19}$$

$$F_{down2riv\_POC} = S_{riv\_POC} \frac{F_{down2riv\_sed\_clay}}{S_{riv\_sed\_clay}} \tag{20}$$

$$F_{riv2fld\_POC} = S_{riv\_POC} \frac{F_{riv2fld\_sed\_clay}}{S_{riv\_sed\_clay}} \tag{21}$$

$$F_{fd\_POC} = S_{fld\_POC} \frac{F_{fd\_sed\_clay}}{S_{fld\_sed\_clay}} \tag{22}$$

$$F_{fld2riv\_POC} = S_{fld\_POC} \frac{F_{fld2riv\_sed\_clay}}{S_{fld\_sed\_clay}} \tag{23}$$

$$F_{bed2fld\_POC} = S_{rivbed\_POC} \frac{F_{bed2fld\_sed}}{S_{rivbed\_sed}} \tag{24}$$

The representation of POC deposition and transformation in the aquatic reservoirs and bed sediment involve as well decomposition, which follows largely the scheme used for SOC (Fig.

438    2a). However, instead of using the rate modifiers for soil temperature and moisture used in the

439    soil carbon module, daily decomposition rates ($F_{POC\_i}$, g C day$^{-1}$) of each POC pool ($S_{POC\_i}$, g C)

440    are simulated to vary with water temperature based on the Arrhenius term which is used to

441    simulate the DOC decomposition in ORCHILEAK (Hanson et al., 2011; Lauerwald et al., 2017):

442    $$F_{POC\_i} = S_{POC\_i} \frac{1.073^{(Twater-28.0)}}{\tau_{poc\_i}}$$    (25)

443    where $T_{water}$ (°C) is the temperature of water reservoirs and is calculated from local soil

444    temperature using an empirical function (Lauerwald et al., 2017). For the POC stored in bed

445    sediment, temperature of the stream reservoir is used to calculate the decomposition rate. $\tau_{POC\_i}$ is

446    the turnover time of the $i$ (active, slow and passive) POC pool. We assumed that the base

447    turnover times of active (0.3 year) and slow (1.12 years) POC pools are the same as for the

448    corresponding SOC pools. The passive SOC pool is generally regarded as the SOC which is

449    associated to soil minerals or enclosed in soil aggregates (Parton et al., 1987). During the soil

450    erosion and sediment transport processes, the aggregates break down and the passive POC loses

451    its physical protection from decomposition (Chaplot et al., 2005; Hu and Kuhn, 2016; Polyakov

452    and Lal, 2008; Wang et al., 2014a). To represent the acceleration of passive POC decomposition

453    due to aggregate breakdown, we assume that the turnover time of the passive POC is same to the

454    active POC (0.3 year), rather than the passive SOC (462 years). Similar to the scheme used to

455    simulate SOC decomposition in ORCHILEAK, the decomposed POC from each of the active,

456    slow and passive pool flows to other POC pools, to DOC pools or is released to the atmosphere

457    as $CO_2$ (Fig. 2). Fractions of the decomposed POC flowing to different POC and DOC pools or

458    to the atmosphere are set to the same values used in ORCHILEAK for simulating the fates of the

459    decomposed SOC pools.

460    Changes in the vertical SOC profile of floodplain soils following sediment deposition is

461    simulated at the end of every daily modelling time-step, after physical transfers and

462    decomposition of POC have been calculated. The sediment deposited on the floodplain becomes

463    part of the surface soil layer, and the active, slow and passive POC flow into the active, slow and

464    passive SOC pools in surface soil layer, respectively. SOC in the original surface and subsurface

465    soil layers is transferred sequentially to the adjacent deeper soil layers. As the vertical soil profile

466    in ORCHILEAK is described by an 11-layer discretization of a 2 m soil column, we introduce a

467 deep (> 2 m) soil pool ($S_{deep}$) to represent the soil and carbon transferred down from the 11th soil

468 layer following ongoing floodplain deposition. Decomposition rates of the organic carbon in this

469 deep soil pool are assumed to be same to those in the 11th (deepest) soil layer.  Note that when

470 the soil erosion rate of the floodplain soil is larger than the sediment deposition rate, sediment

471 and organic carbon in $S_{deep}$ move up to replenish the stocks of the 11th soil layer.

## 2.3 Model application and evaluation

473 In this study, ORCHIDEE-C$_{lateral}$ was applied over Europe and parts of Middle East (-30W– 70E,

474 34N-75N), where extensive observation datasets are available to calibrate and evaluate our

475 model (Table 1). The return period of daily bankfull flow ($P_{flooding}$, year), which represents the

476 average interval between two flooding events and is used in this study to produce the forcing file

477 of $S_{rivmax}$ from a pre-run of ORCHILEAK. Note that $P_{flooding}$ is generally shorter than the return

478 period of real flooding events, as the flooding may occur in several continuous days and all the

479 flooding waters occurring on these continuous days are generally regarded to belong to the same

480 flooding event (supplementary Fig. S2). To our knowledge, existing observational data on

481 $P_{flooding}$ are still very limited. Therefore, following Schneider *et al*. (2011), we also use a constant

482 $P_{flooding}$ to simulate the bankfull flows from European rivers and the observed long-term (1961–

483 2000) average bank full flow rate (m$^3$ s$^{-1}$) at 66 sites obtained from Schneider *et al*. (2011) was

484 used to calibrate $P_{flooding}$ (the optimized value is 0.1 year, Table 2). To our knowledge, there is

485 still no large-scale observation data on the sediment delivery rates from land to river networks in

486 Europe to our knowledge. Therefore, following Zhang et al. (2020), the parameters a, b, c and d

487 in Eq. 1 and 2 (Table 2) were calibrated at for 57 European catchments (Fig. S3d) against the

488 modelled sediment delivery data obtained from the European Soil Data Centre (ESDAC, Borrelli

489 et al., 2018). The sediment delivery data from the ESDAC product is simulated by thewas

490 derived from WaTEM/SEDEM model simulations using high-resolution data of topography, soil

491 erodibility, land cover and rainfall. It has beenThis model was calibrated and validated using

492 observed sediment fluxes from 24 European catchments (Borrelli et al., 2018).

493 Parameters controlling sediment transport, deposition and re-detachment (i.e. $\omega$, $c_{rivdep}$, $c_{flddep}$,

494 $c_{ebed}$ and $c_{ebank}$, Table 2) in stream and flooding reservoirs were calibrated against the observed

495 long-term averaged sediment discharge rate (Table 1). We also conducted a sensitivity analysis

496 to test the sensitivity of the simulated riverine sediment and carbon discharges to these

497     parameters, following the method used in Tian et al. (2015). The sensitivity of simulation results

498     was evaluated based on the relative changes in simulated riverine sediment and carbon

499     discharges to a 10% increase and decrease of each parameter (Table 2). Result of the sensitivity

500     analysis shows that the simulated riverine sediment and POC discharges are most sensitive to

501     $c_{rivdep}$ in Eq. 10, followed by $\omega$ in Eq. 8 (Fig. S4). Compared to $c_{rivdep}$ and $\omega$, the simulated

502     riverine sediment and POC discharges are less sensitive to $c_{flddep}$, $c_{ebed}$ and $c_{ebank}$. With 10%

503     changes in $c_{flddep}$, $c_{ebed}$ or $c_{ebank}$, the changes in riverine sediment and POC discharges are

504     generally less than 3%. In addition, the changes in simulated riverine DOC and $CO_2$ discharges

505     are mostly less than 1% with 10% changes in $\omega$, $c_{flddep}$, $c_{ebed}$ and $c_{ebank}$. Nonetheless, a 10%

506     change in $c_{rivdep}$ can lead to a change of about 5% in the simulated riverine $CO_2$ discharge (Fig.

507     S4).

508     **Table 2** Values of the key parameters used in the ORCHIDEE-C$_{lateral}$ to simulate the lateral

509     transfer of sediment and carbon.

| Parameter | Value | Unit | Description | Source |
|---|---|---|---|---|
| $a$ | 26.96 | Unitless | Coefficient in Eq. 1 | Calibrated |
| $b$ | 0.76 | Unitless | Coefficient in Eq. 1 | Calibrated |
| $c$ | 1.79 | Unitless | Coefficient in Eq. 2 | Calibrated |
| $d$ | -0.065 | Unitless | Coefficient in Eq. 2 | Calibrated |
| $c_{ebed}$ | 0.5 | Unitless (0-1) | The fraction of sediment deficit that can be complemented by erosion of river bed (Eq. 6) | Calibrated |
| $c_{ebank}$ | 0.5 | Unitless (0-1) | The fraction of sediment deficit that can be complemented by erosion of river bank (Eq. 6) | Calibrated |
| $c_{rivdep}$ | 0.1, 0.2, 0.5[a] | Unitless (0-1) | Daily deposited fraction of the sediment surplus in stream reservoir (Eq. 5) | Calibrated |
| $c_{flddep}$ | 0.5, 1.0, 1.0[a] | Unitless (0-1) | Daily deposited fraction of the sediment surplus in flooding reservoir (Eq. 11) | Calibrated |
| $P_{flooding}$ | 0.1 | year | Return period of daily bankfull flow | Calibrated |
| $\tau_{fast}$ | 3.0 | day | A factor which translates the topographic index into the water residence time of the 'fast' reservoir (Eqs. 5, 6) | Guimberteau et al., 2012 |

| | | | | |
|---|---|---|---|---|
| $\tau_{flood}$ | 1.4 | day | A factor which translates the topographic index into the water residence time of the flooding reservoir (Eq. 18) | Guimberteau et al., 2012 |
| $\tau_{poc}$ | 0.3, 1.12, 0.3[b] | year | A factor which translates the topographic index into the water residence time of the flooding reservoir (Eq. 25) | Lauerwald et al., 2017 |
| $\omega$ | 12.0, 5.0, 2.5[a] | g s$^{-1}$ | Coefficient of proportionality for calculating sediment transport capacity (Eq. 8) | Calibrated |

510    [a] For clay, silt and sand sediment, respectively. [b] For active, slow and passive POC, respectively.

511

512    After parameter calibration, ORCHIDEE-C$_{lateral}$ was applied to simulate the lateral transfers of

513    water, sediment and organic carbon in European rivers over the period 1901-2014. Before this

514    historical simulation, ORCHIDEE-C$_{lateral}$ was run over 10,000 years (spin-up) until the soil

515    carbon pools reached a steady state. In the 'spin-up' simulation, the PFT maps, atmospheric $CO_2$

516    concentrations and meteorological data during 1901–1910 were used repeatedly as forcing data.

517    The finally simulated water discharge rates in European rivers were evaluated using observation

518    data at 93 gauging sites (locations see Fig. S3a) from the Global Runoff Data Base (GRDC,

519    Table 1). The simulated bankfull flows were evaluated against observed long-term (1961–2000)

520    average bankfull flows at 66 sites (Fig. S3b) from Schneider *et al*. (2011). The simulated riverine

521    sediment discharge rate is evaluated using observation data from the European Environment

522    Agency and existing publications (see Table 1) at 221 gauging sites (Fig. S3c). The riverine total

523    organic carbon (TOC), POC and DOC concentrations provided by the GLObal RIver Chemistry

524    Database (GLORICH, Hartmann et al., 2019) at 346 sites (Fig. S3d) were used to evaluate the

525    simulated riverine POC and DOC concentrations. Note that observations in the GLORICH

526    database which are measured at gauging sites with drainage area $<1.0\times10^4$ km$^2$ were excluded

527    from our model evaluation, because these small catchments cannot be represented by the coarse

528    river network scheme at 0.5 degree (ca. 55 km at the equator). Among the retained 346 gauging

529    sites, TOC concentrations were measured at 188 sites, DOC was measured at 314 sites. POC was

530    measured at only two sites (Bad honnef (51 measurements) and Bimmen (78 measurements)) in

531    the Rhine catchment and one site (Rheine, 36 measurements) in the Ems catchment (Fig. S3d).

532    **3 Results and Discussion**

533    **3.1 Model evaluation**

### 3.1.1 Stream water discharge and bankfull flow

Evaluation of our simulation results using *in situ* observation data from Europe rivers indicates that ORCHIDEE-C$_{lateral}$ well reproduces the magnitude and interannual variation of water discharge rates in major European rivers (Figs. 3a and S5). Overall, the simulated riverine water discharge rate explained 94% (Fig. 3a) of the spatial variation of the observed long-term average water discharge rates across 93 gauging sites in Europe (Fig. S3a). Relative biases (calculated as: $\frac{simulation-observation}{observation} \times 100\%$, as used through the manuscript if not otherwise stated) of the simulated average water discharge rates compared to the observations are mostly smaller than 30% (Fig. 3a). For major European rivers, such as the Rhine, Danube, Elbe, Rhone and Volga, ORCHIDEE-C$_{lateral}$ also captures the interannual variation of the water discharge rate (Fig. S5). We recognize that ORCHIDEE-C$_{lateral}$ may overestimate or underestimate the water discharge rate in some rivers (Fig. 3a), particularly in smaller rivers where discrepancy between the stream routing scheme (delineation of catchment boundaries) extracted from the forcing data at 0.5° resolution and the real river network (Fig. S6) can be substantial. An over-estimation or underestimation of the catchment area by the forcing data as respectively found for the Elbe and Rhine will introduce a proportional bias in the average amount of simulated discharge from these catchments. Another problem are stream channel bifurcations which occur in reality, but which are not represented in a stream network derived from a digital elevation model. For example, in the Danube river delta, a fraction of the discharge is actually exported to the sea through the Saint George Branch, in addition to the water discharge through the main river channel (Fig. S6b). This explains why the simulated water discharge rate at the outlet of the Danube catchment is larger than the observation at the Ceatal gauging station, Romania (identify number in the GRDC database is 6742900, Fig. S5m), where only the main stream discharge was measured.

557
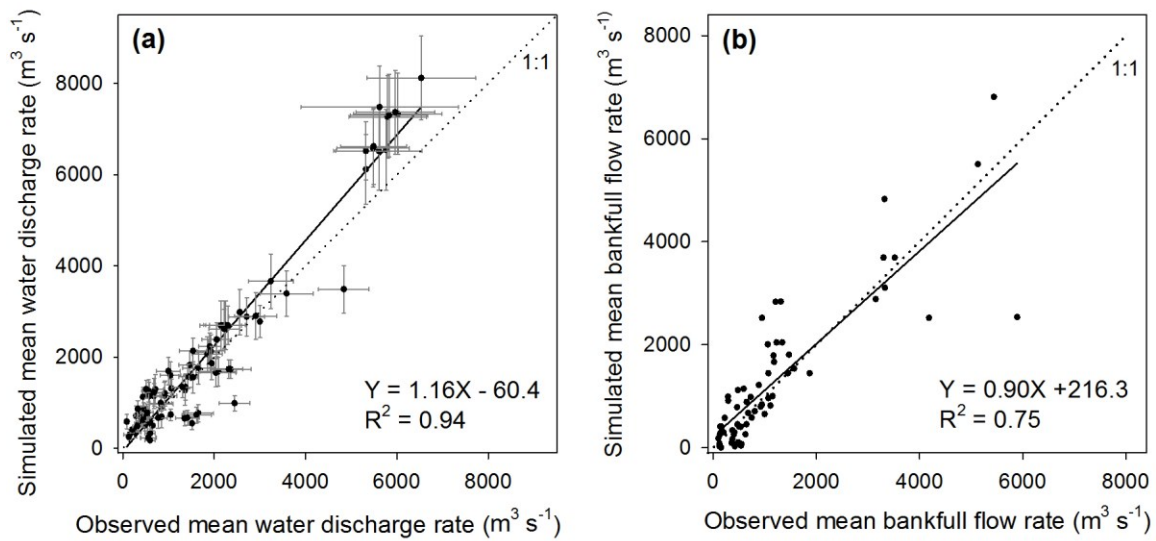
**Figure 3** Comparison between observed and simulated riverine water discharge rates (a) and bankfull flow rates (b). In figure (a), the error bar denotes the standard deviation of interannual variation. Sources of the observed riverine water discharge rate and bankfull flow rate can be found in Table 1.

With the calibrated return period (= 0.1 year) of the daily flooding rate (see section 2.3), the simulated bankfull flow rates compare well to observations at the 66 sites for which data was available (Fig. 3b). Overall, the simulation result explained 75% of the inter-site variation of the observed bankfull flow rates. Relative biases of the simulated bankfull flow rates are generally lower than 30%, although the relative bias may be larger than 100% at some sites.

**3.1.2 Sediment transport**

The simulated area-averaged sediment delivery rates from upland to river network by the ORCHIDEE-$C_{lateral}$ are overall comparable to those simulated by the WaTEM/SEDEM for most catchments in Europe (Figs. 4a and S3d). In the two catchments in the Apennine Peninsula, ORCHIDEE-$C_{lateral}$ gives a drastically lower estimation on the sediment delivery rates compared to WaTEM/SEDEM. By excluding these two catchments, ORCHIDEE-$C_{lateral}$ reproduces 72% of the spatial variation of the sediment delivery rates estimated by the WaTEM/SEDEM (Fig. 4a). In addition, the average sediment loss rate over all catchments showed in Fig. S3d is 40.8 g m$^{-2}$ yr$^{-1}$, which is overall comparable to the estimate by the WaTEM/SEDEM (42.5 g m$^{-2}$ yr$^{-1}$).

576    ORCHIDEE-C$_{lateral}$ reproduces 83% of the inter-site variation of the observed riverine sediment

577    discharge rates across Europe (Fig. 4b). Simulation of the riverine sediment discharge rate at

578    large spatial scale is still a big challenge. It generally needs detailed information on the stream

579    flow, geomorphic properties of river channel and the particle composition of the suspended

580    sediment (Neitsch et al., 2011). Moreover, the parameters of existing sediment transport models

581    usually require recalibration when they are applied to different catchments (Gassman et al.,

582    2014; Oeurng et al., 2011; Vigiak et al., 2017). In ORCHIDEE-C$_{lateral}$, the sediment processes in

583    river networks are simulated using simple empirical functions and parameters based on a routing

584    scheme at a spatial resolution of 0.5° (section 2.2.1). Detailed information about the stream flow

585    (e.g. cross-sectional area) and the geomorphic properties of river channels are not represented.

586    Sediment discharge in all catchments was simulated using a universal parameter set. This may

587    explain why ORCHIDEE-C$_{lateral}$ fails to capture the observed sediment discharge rates in some

588    specific catchments, especially those with relatively small drainage areas (e.g. $< 5 \times 10^3$ km$^2$).
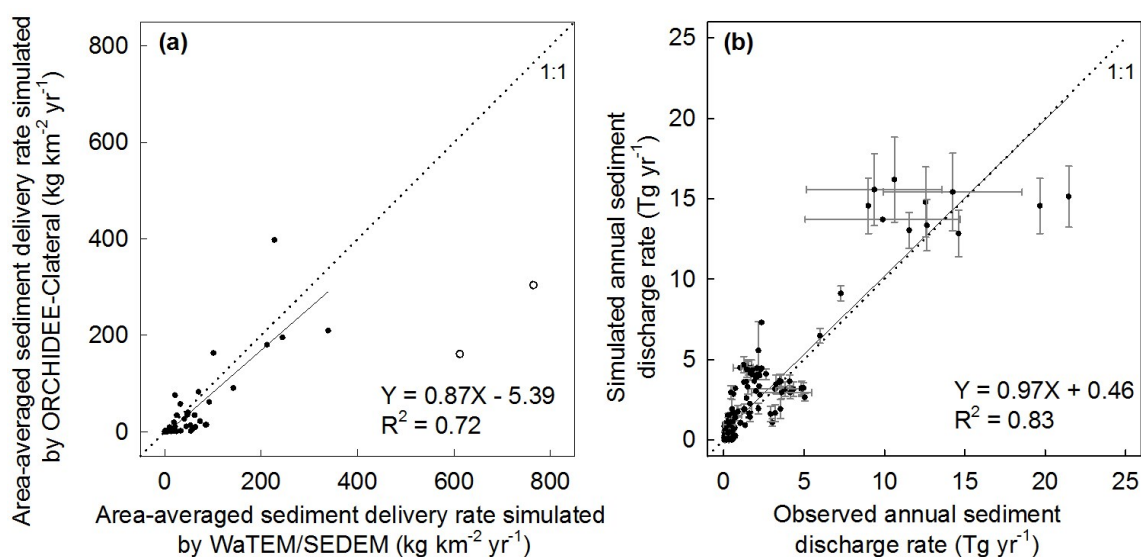
589

590    **Figure 4** Comparison between the simulated area-averaged sediment delivery rate from uplands

591    to river network from ORCHIDEE-C$_{lateral}$ and WaTEM/SEDEM (a), and the comparison between

592    observed and simulated annual sediment discharge rates at 221 gauging sites (b). In figure (a),

593    the two hollow dots represent the sediment delivery rates at the two catchments in the Apennine

594    Peninsula (Fig. S3d). The regression function in figure (a) was obtained based on the values of

595    all solid dots, excluding the two hollow dots. In figure (b), the error bar denotes the standard

596 deviation of interannual variation. Sources of the observed annual sediment discharge rate in
597 Table 1.

**3.1.3 Organic carbon transport**

599 Simulation of the riverine carbon discharge rate at large spatial scale is even a bigger challenge
600 than simulating sediment discharge, as the riverine carbon discharge is controlled by many
601 factors, such as upland topsoil SOC concentrations, soil erosion rate, transport and deposition
602 rate of clay fraction in river channel and on floodplain, and the decomposition of POC in transit
603 and in aquatic sediments.  As described above, the simulated water discharge rate, bankfull flow
604 and sediment discharge rate are overall comparable to observation (Figs. 3 and 4). The simulated
605 total SOC stock in the top 0-30 cm soil layer in Europe of 107 Pg C is close to the value
606 extracted from the HWSD database (106 Pg C), but significantly lower than the values extracted
607 from some other databases, such as the GSDE (249 Pg C), SoilGrids (202 Pg C), S2017 (148 Pg
608 C) and landGIS (226 Pg C) (Fig. S7a). We noticed that the SOC stocks extracted from these
609 observation-based soil databases show considerable difference (vary from 106 to 249 Pg C), as
610 they have been produced using different clusters of site-level SOC measurements and different
611 interpolation methods to produce global gridded SOC stocks from the site-level measurements
612 (Shangguan et al., 2014; Hengl et al., 2014; Sanderman et al., 2017). Distribution of the
613 simulated SOC stock along the latitude gradients ($30° N – 75° N$) are overall comparable to
614 those extracted from the HWSD and S2017 databases (Fig. S7). But even compared to these two
615 databases, our model still underestimated the SOC stock in southern Europe ($30° N – 41° N$).

616 Comparison of the simulated concentrations of riverine organic carbon and the observations
617 obtained from the GLORICH database (Hartmann et al., 2019) indicates that our model can
618 basically capture the TOC and DOC concentrations in European rivers (Figs 5, 6, S8 and S9).
619 The simulation results explain 34% and 32% of the inter-site variation of the observed TOC and
620 DOC concentrations, respectively (Fig. 5). For major European rivers, such as the Rhine, Elbe,
621 Danube, Spree and Weser, the simulated long-term average TOC and DOC concentrations are
622 overall close to the observations (Figs. 6, S8 and S9). But for the Rhone river in southern France,
623 the DOC concentrations have been systematically overestimated by more than 50% (Figs. 6 and
624 S9m). In addition, both simulated and observed TOC and DOC concentrations show drastic
625 temporal (both seasonal and interannual) variations (Figs 5, S8 and S9). Our model seems to

626 have overestimated the temporal variation of TOC and especially DOC concentrations (Figs. S8

627 and S9). Nonetheless, the simulated temporal variation of TOC and DOC discharge rates are

628 overall comparable to the observation (Figs. S10 and S11), as our model can well capture the

629 magnitude and temporal variation of riverine water discharge rates.
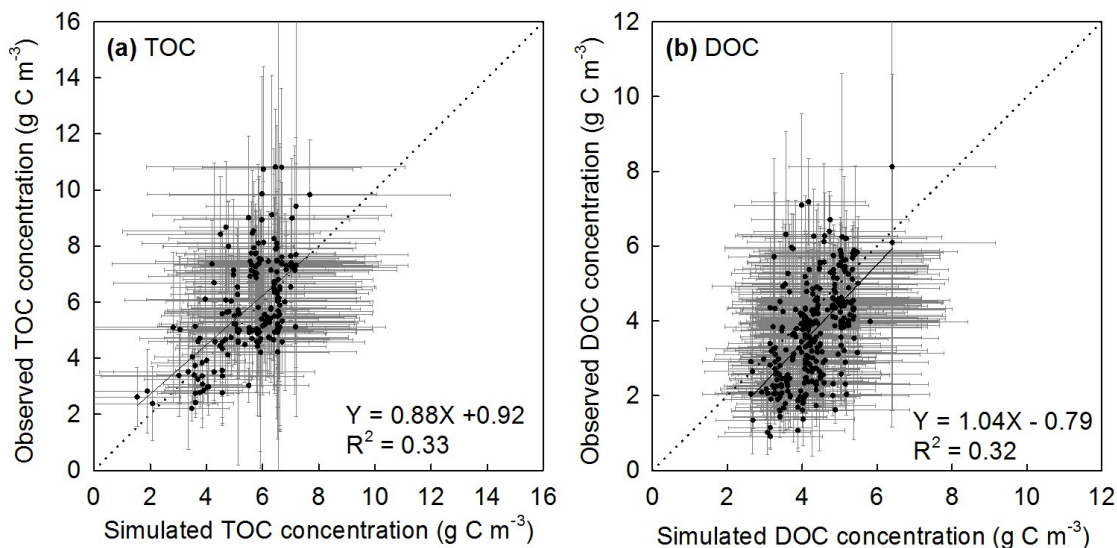
630

631 **Figure 5** Comparison between the observed and simulated riverine TOC (a, POC+DOC) and

632 DOC (b) concentrations. The dot and error bar denote the mean and standard deviation at each

633 gauging site, respectively. Note that the mean and standard deviation of the simulated

634 concentrations at each site are calculated based on the monthly average value, but the mean and

635 standard deviation of the observed concentrations are based on instantaneous observation.

636
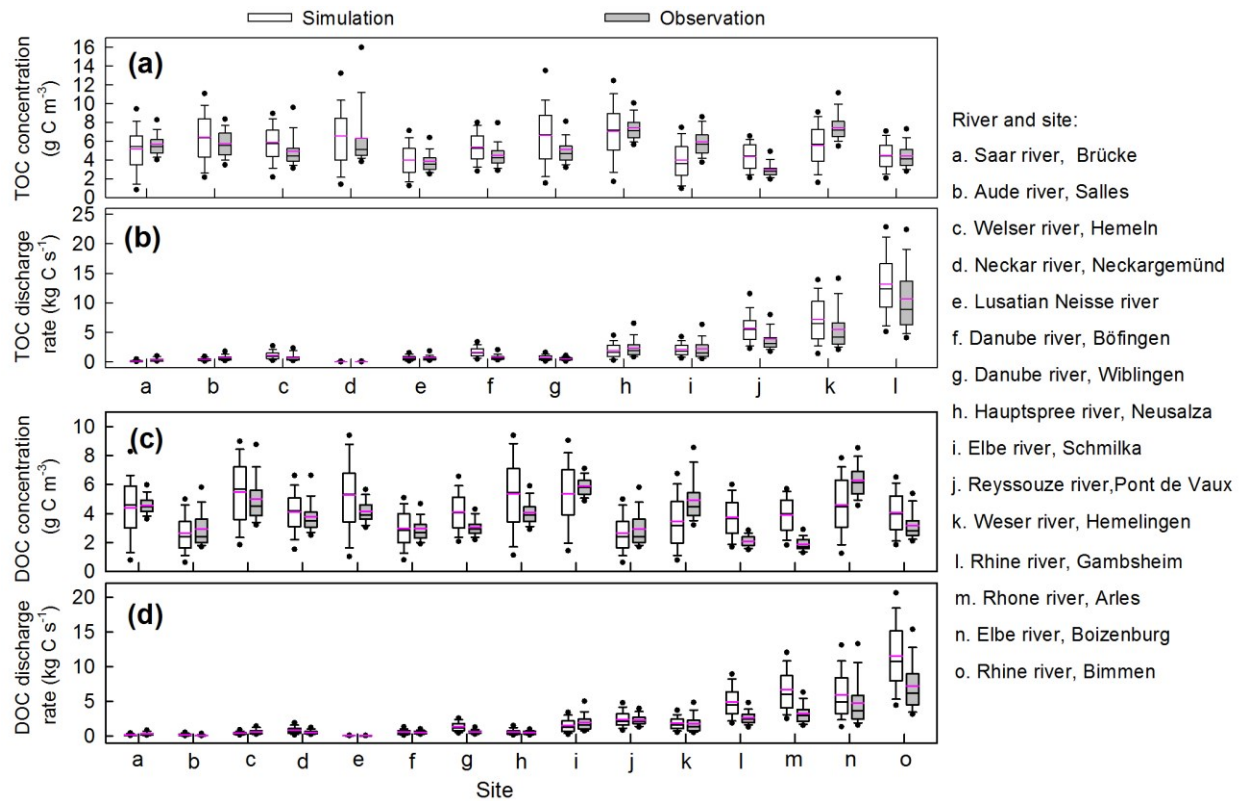
**Figure 6** Comparison between the observed and simulated concentrations of total organic carbon (TOC, a) and dissolved organic carbon (DOC, b) in river flows, as well as the discharge rates of riverine TOC and DOC. The black and pink lines in each box denote the median and mean value, respectively. Box boundaries show the 25th and 75th percentiles, whiskers denote the 10th and 90th percentiles, the dots below and above each box denote the 5th and 95th percentiles, respectively.

In Europe, the GLORICH database only provides POC concentrations measured at three gauging stations in northwestern Germany (Figs. 7, S3d). The simulated POC concentrations and discharge rates in the Ems river at Rheine are overall comparable to the observation (Figs. 7e,f). However, at the two gauging sites at the river Rhine, the POC concentrations have been significantly underestimated (Figs. 7a-d). We noticed that the stream routing scheme of Rhine catchment at 0.5° obtained from the forcing data STN-30p (Vörösmarty et al., 2000) differs significantly from the stream routing scheme extracted based on high resolution (3″) DEM (Fig. S6). Thus, besides the errors in simulated SOC stocks, soil erosion rate, stream discharge rate, and sediment transport and deposition rate, the inaccurate stream routing scheme used in this study might also be an important reason for the underestimation of POC concentration in Rhine river.
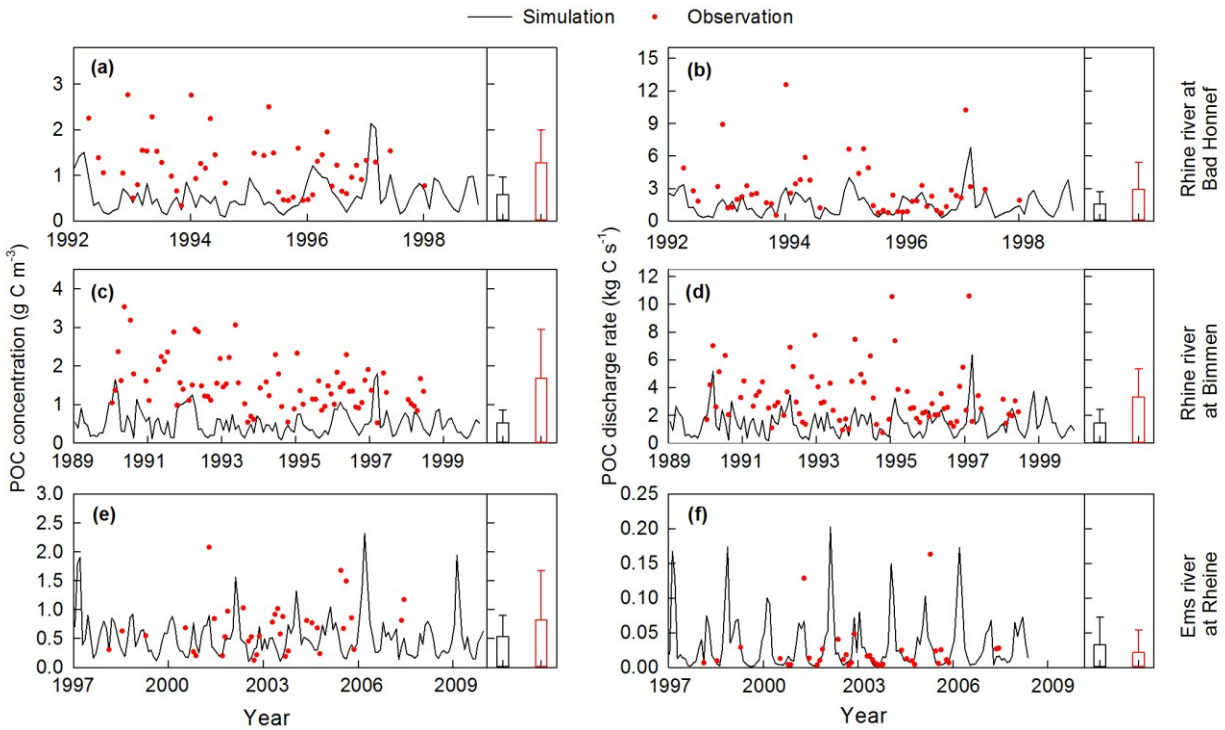
653

654    **Figure 7** Comparison between observed (instantaneous measurements) and simulated (monthly

655    average values) riverine POC concentrations and POC discharge rates at three gauging sites. The

656    histograms and error bars denote the means and standard deviations of POC concentrations,

657    respectively. Long-term average water discharge rates at Bad Honnef, Bimmen and Rheine

658    during the observation periods are 2023, 2100 and 80 $m^3$ $s^{-1}$, respectively.

659    **3.2 Lateral carbon transfers in Europe**

660    Based on our simulation results, the average annual sediment delivery from upland to the river

661    network caused by water erosion in Europe (-30W– 70E, 34N-75N) during 1901-2014 is 2.8±0.4

662    Pg $yr^{-1}$ (Fig. 8a). From Northern to Southern Europe, the sediment delivery rate from upland to

663    river increase from less than 1.0 g $m^{-2}$ $yr^{-1}$ in the Scandinavia Peninsula, which is covered by

664    mature boreal forests (Fig. S12a), and in the Northern European Plain to more than 600 g $m^{-2}$ $yr^{-1}$

665    in the mountainous regions of the Apennine Peninsula, Balkan Peninsula and the Middle East

666    (Figs. 9a, S13a). In total across Europe, 63.2% (1.8±0.2 Pg $yr^{-1}$) of the sediment delivered into

667    river network is deposited in river channels and floodplains, and the remaining 36.8% (1.0±0.1

668    Pg $yr^{-1}$) is exported to the sea (Fig. 8a). Generally, large rivers, like Danube, Volga, and Ob

669    rivers, carry more sediment to the sea than small rivers (Figs. 9b, c). But several relatively small

670 rivers in the Middle East and the Po river in northern Italy also carry similarly large amount of

671 sediment to the sea, as the upland soil erosion rates are very high ($> 200$ g m$^{-2}$ yr$^{-1}$) in these

672 catchments (Figs. 9a, c). Spatial distribution of the sediment deposition is controlled by the

673 stream routing scheme and the spatial distribution of floodplains (Fig. 10b). In Northern and

674 Central Europe, the area-averaged sediment deposition rates (i.e. amount of annual sediment

675 deposition /area of $0.5° \times 0.5°$ grid cell) in river channels and floodplains are mostly less than

676 100.0 g m$^{-2}$ yr$^{-1}$ (Fig. 9d). In the downstream part of the Danube, Po and several rivers in the

677 Middle East, the sediment deposition rate can exceed 800.0 g m$^{-2}$ yr$^{-1}$. From 1901 to 1960s, the

678 annual total sediment delivery from uplands to the whole river network of Europe declined

679 significantly ($p<0.01$, independent sample t-test) from about 3.0 Pg yr$^{-1}$ to about 2.3 Pg yr$^{-1}$ (Fig.

680 S14a). From 1960 to 2014, the annual sediment delivery rate did not show a significant trend, but

681 revealed large interannual variations.
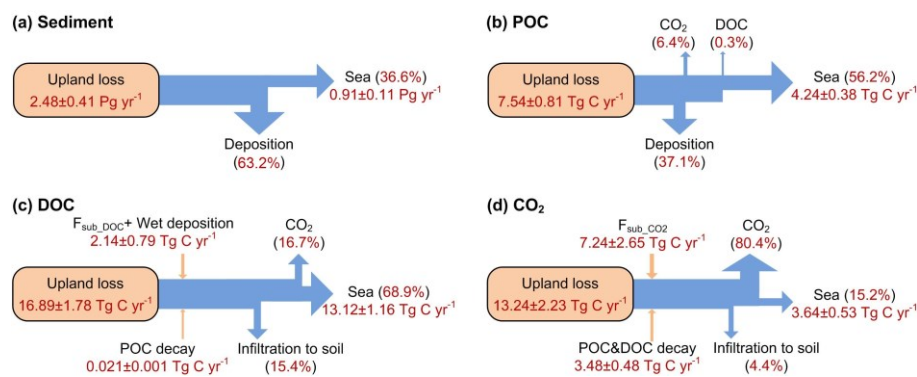
682

683 **Figure 8** Averaged annual lateral redistribution rate of sediment (a), POC (b), DOC (c) and $CO_2$

684 (d) in Europe for the period 1901-2014. $F_{sub\_DOC}$ and $F_{sub\_CO2}$ are the DOC and $CO_2$ inputs from

685 floodplain soil (originated from the decomposition of submerged litter and soil carbon) to the

686 overlying flooding water, respectively.
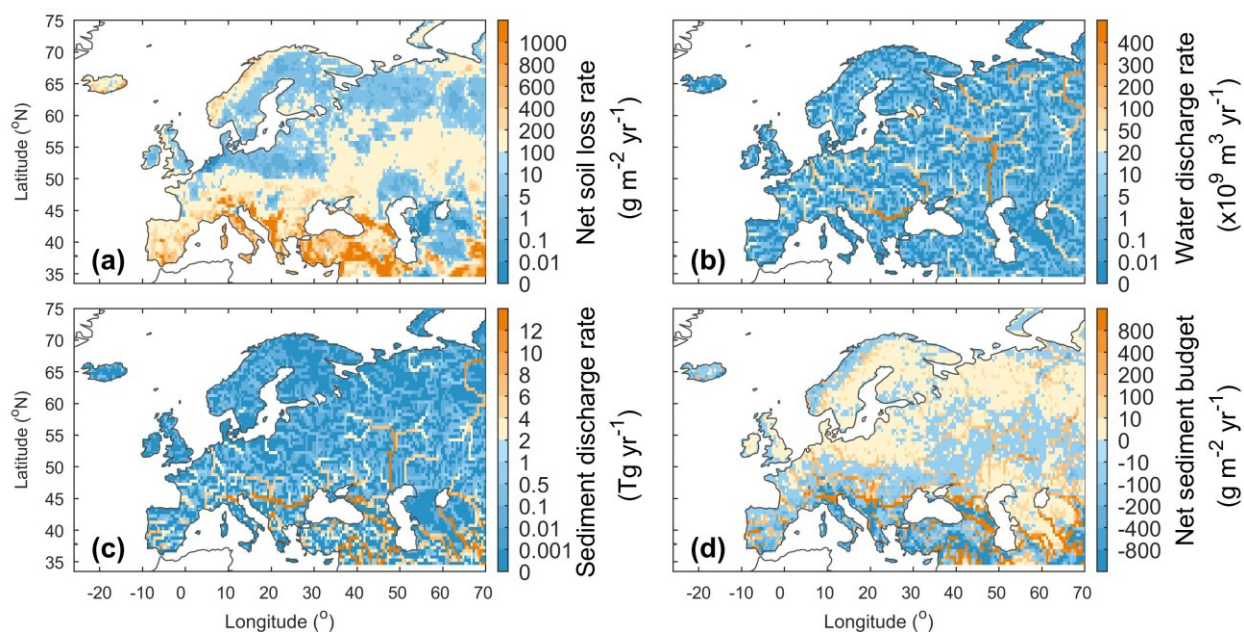
**Figure 9** Averaged annual lateral redistribution rate of water and sediment in Europe during 1901-2014. (a) Annual sediment delivery rate from upland to river network; (b) annual water discharge rate; (c) annual sediment discharge rate and (d) annual net sediment budget in each 0.5°×0.5° grid cell. In figure d, the positive and negative values denote net gain and net loss of sediment, respectively.

Along with soil erosion and sediment transport, the average annual POC delivery from upland to river network in the whole Europe during 1901-2014 is 10.1±1.1 Tg C yr$^{-1}$ (Fig. 8b). 41.0% of the POC delivered into the river network is deposited in river channels and floodplains, 2.9% is decomposed during transport, and the remaining 56.1% is exported to the sea. Spatial patterns of the area-averaged SOC delivery rate and POC discharge rate basically follow that of sediment (Fig. 10a, c). Although the sediment discharge rates in some rivers in the Middle East can be as high as that in the Danube or Volga river (Fig. 9c), the POC delivery rates in these rivers are much smaller than in the larger ones (Fig. 10c). This is mainly due to the lower SOC stocks in the Middle East compared to those found in the Danube and Volga catchments (Fig. S7). We also note that different from the sediment delivery, the annual total POC delivery from upland to river network in Europe did not show a significant declining trend from 1901 to 1960s (Fig. S14b). The increase in SOC stock (Fig. S14c) may have partially offset the decline in sediment delivery rate.

706
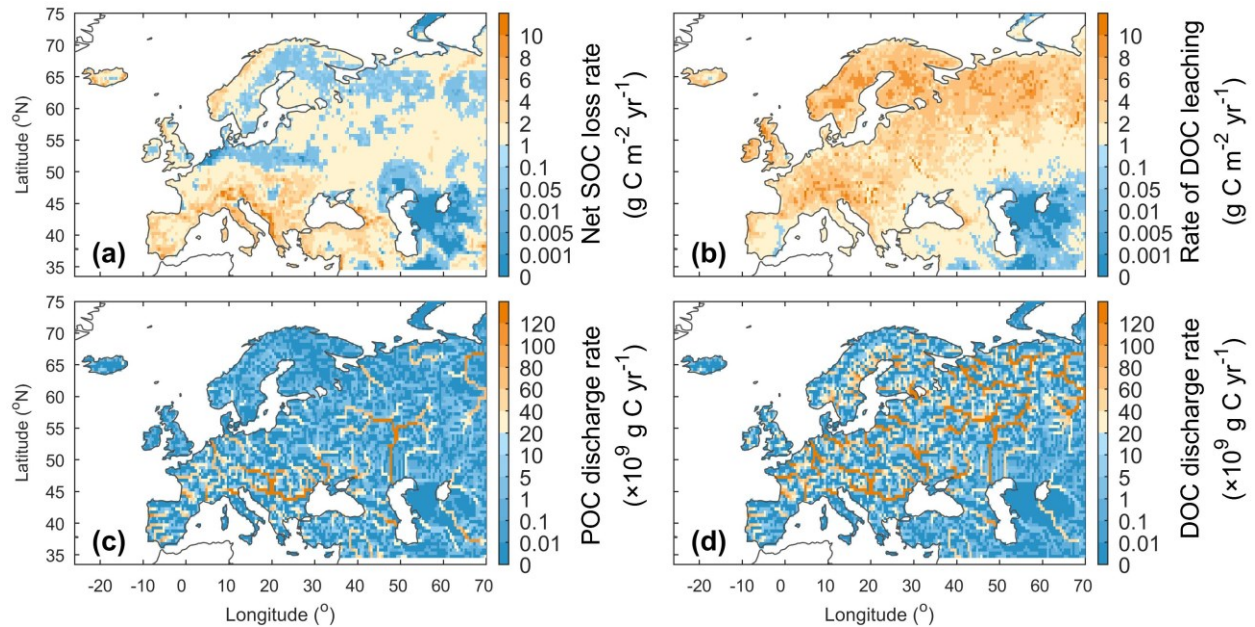
**Figure 10** Averaged annual lateral redistribution rate of organic carbon in Europe during 1901-
2014. (a) Annual SOC delivery rate from upland to river network; (b) annual DOC leaching rate;
(c) annual POC discharge rate and (d) annual DOC discharge rate.

Leaching results in an average annual DOC input of $13.5\pm1.5$ Tg C yr$^{-1}$ from soil to the river
network in Europe, and the *in-situ* DOC production caused by wet deposition and the
decomposition of riverine POC and submerged litter and soil organic carbon under flooding
waters amounts to $2.2\pm0.7$ Tg C yr$^{-1}$ (Fig. 8c). 28.1% of the total riverine DOC is then infiltrating
into the floodplain soils, 12.9% is decomposed during riverine transport, and the remaining
59.0% is exported to the sea. The spatial distribution of the DOC leaching rate is very different
from that of POC (Fig. 10b). From North-western Europe to Southeast Europe and the Middle
East, the DOC leaching rates decrease from over 6 g C m$^{-2}$ yr$^{-1}$ to less than 1.0 g C m$^{-2}$ yr$^{-1}$. DOC
discharge rates in major European rivers, such as Rhine, Danube, Volga, Elbe and Ob, are mostly
higher than 100 Tg C yr$^{-1}$ (Fig. 10d). Comparatively, the DOC discharge rates in Southern
Europe and the Middle East are significantly lower (<60 Tg C yr$^{-1}$).

The average annual leaching rate of $CO_2$ sourced from the decomposition of upland litter and
soil organic carbon (incl. DOC) in the whole Europe is $14.3\pm2.2$ Tg C yr$^{-1}$ (Fig. 8a).
Decomposition of the submerged litter and organic carbon in floodplains and the decomposition
of riverine POC and DOC add an an *in-situ* $CO_2$ production amounting to $7.5\pm2.7$ Tg C yr$^{-1}$ and

725 $4.1 \pm 0.5$ Tg C yr$^{-1}$, respectively. Most of this $CO_2$ (80.2%) feeding stream waters is then released

726 back to the atmosphere quickly, in such a way that only 15.8% of the $CO_2$ is exported to the sea,

727 and 4.0% is infiltrated into the floodplain soils.

**3.3 Implications for the terrestrial C budget of Europe**

729 Representing the lateral carbon transport in LSM is helpful to estimate the terrestrial carbon

730 cycle more accurately. From the year 1901 to 2014, soil erosion and leaching combined resulted

731 in a 5.4 Pg loss of terrestrial carbon to the European river network, this amount corresponding to

732 about 5% of the total SOC stock (106 Pg C, Fig. S7a) in the 0-30 cm soil layer. The average

733 annual total delivery of organic carbon (POC+DOC) during the same period is $47.3 \pm 6.6$ Tg C yr$^{-1}$

734 (Fig. 8), which is about 4.7% of the net ecosystem production (NEP ($993 \pm 255$ Tg C yr$^{-1}$),

735 defined as the difference between the vegetation primary production (NPP) and the soil

736 heterotrophic respiration (Rh) due to the decomposition of litter and soil organic matter, i.e.

737 NEP=NPP–Rh), and 19.2% of the net biome production (NBP ($243 \pm 189$ Tg C yr$^{-1}$), defined as

738 the difference between NEP and the land carbon loss (Rd) due to the additional disturbances (e.g.

739 harvest, land cover change, and soil erosion and leaching, i.e. NBP=NEP–Rd–DOC and POC to

740 river) (Fig. 11b). The annual total export of carbon to the sea surrounding Europe is $19.0 \pm 1.4$ Tg

741 C yr$^{-1}$, which amounts to 1.9% and 8.7% of the NEE and NBP, respectively.
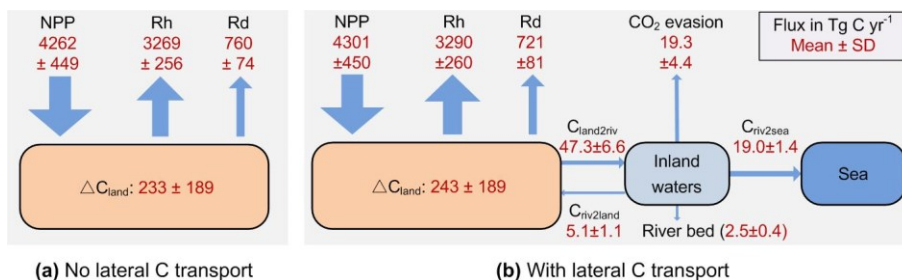
**Figure 11** The simulated average annual carbon budget of the terrestrial ecosystem in Europe

744 during the 1901-2014 when the lateral carbon transport is ignored (a) and considered (b). All

745 fluxes are presented as mean ± standard deviation. NPP is the net primary production. Rh and Rd

746 are the heterotrophic respiration and the respiration due to disturbances like harvest and land

747 cover change, respectively. $\Delta C_{land}$ is the average annual changes of the total land carbon stock.

748 Percentage following each of these changes in blue is the average annual relative changes of the

749 corresponding carbon pool. $C_{land2riv}$, $C_{riv2land}$ and $C_{riv2sea}$ are the average annual carbon fluxes

750    from land to inland waters, from inland waters to floodplains and from inland waters to the sea,

751    respectively. SD is the standard deviation.

752    Besides direct transfers of organic carbon from soil to aquatic systems, the lateral transport of

753    water, sediment and carbon can also affect the land carbon budget through several indirect ways.

754    First, the lateral redistribution of surface runoff can affect the land carbon budget by altering soil

755    wetness. Our simulation results reveal that the lateral redistribution of runoff can significantly

756    change local soil wetness, especially in floodplains (Fig. S13b), where the increase in soil

757    wetness can be larger than 10% (Fig. S16b). Soil wetness is a key controlling factor of plant

758    photosynthesis (Knapp et al., 2001; Stocker et al., 2019; Xu et al., 2013). Benefiting from the

759    increase in soil wetness, the NPP in many grid cells with a large area of floodplain has increased

760    by more than 5% (Fig. 11b), although the NPP over the whole Europe only increased by 1%

761    (Fig. 11). Changes in soil wetness can further alter soil temperature (Fig. S16a). As soil wetness

762    and temperature are the two most important controlling factors of organic matter decomposition,

763    the lateral redistribution of runoff can affect local land carbon budget by changing the Rh.

764    Moreover, in ORCHIDEE-C$_{lateral}$, the turnover times of litter and SOC under flooding waters

765    (assumed to experience anaerobic condition) are set to be one third of the litter and SOC turnover

766    times in upland soil (Reddy & Patrick Jr, 1975; Neckles & Neill, 1994; Lauerwald et al., 2017).

767    Accounting for flooding thus decreases the decomposition rate of litter and SOC stored in

768    floodplain soils.

769    Second, soil erosion and sediment deposition can affect land carbon budget by altering the

770    vertical distribution of litter and soil organic carbon. At the net erosion sites of the uplands, the

771    loss of surface soil results in a part of the belowground litter and SOC that were originally stored

772    in deeper soil layers emerging to the surface soil layers, and also results in a fraction of the

773    belowground litter becoming the aboveground litter. In the floodplains, the newly deposited

774    sediment becomes part of the surface soil layer, and the belowground litter and SOC in the

775    original surface soil layer is transferred down to the deeper soil layers. As the temperatures and

776    fresh organic matter inputs (sourced from the aboveground litterfall and dead roots), which can

777    impact SOC decomposition rates through the priming effect (Guenet et al., 2016; Guenet et al.,

778    2010), in different soil layers are different, changes in the vertical distribution of belowground

779      litter and SOC can therefore lead to changes in the overall decomposition rate of the organic

780      matter in the whole soil column.

781      Third, soil aggregates mostly break down during soil erosion and sediment transport, the riverine

782      POC thus loses part of its physically protection from decomposition (Hu and Kuhn, 2016; Lal,

783      2003). Some modelling studies have assumed that at least 20% of the eroded SOC would be

784      decomposed during the soil erosion and transport processes (Lal, 2003, 2004; Zhang et al.,

785      2014). However, the estimation by Smith et al. (2001) using a conceptual mass balance model

786      suggest that only a tiny fraction of the eroded POC is decomposed and released as $CO_2$ to the

787      atmosphere. Using laboratory rainfall-simulation experiments, van Hemelryck et al. (2010)

788      estimated a 2%-12% mineralization of the eroded SOC from a loess soil, and Wang et al. (2014)

789      estimated a mineralization of only 1.5%. In ORCHIDEE-$C_{lateral}$, the passive SOC pool is

790      regarded as the SOC associated to soil minerals and protected by soil aggregates. The turnover

791      time of the passive POC in river stream and flooding waters is assumed to be same to that of the

792      active POC (0.3 year). Our simulation results suggest that the fraction of total riverine POC that

793      is decomposed during the lateral transport from uplands to the sea is 2.9% in Europe (Fig. 8b),

794      which is larger than the POC decomposition fraction (0.9%) when the turnover time of the

795      passive POC in rivers is assumed to be same to that of the passive POC (i.e. no soil aggregates

796      break down). The acceleration of POC decomposition rate due to the breakdown of soil

797      aggregates can thus slightly affect the estimate of the regional land-atmosphere carbon flux.

798      Moreover, the riverine POC and DOC can be transported over a long distance and finally settle

799      or infiltrate in floodplains or river channels (especially the Estuarine deltas) where the local

800      environmental conditions might be quite different from those encountered  in the uplands from

801      where these C pools originate. These changes in environmental conditions can affect the

802      decomposition rate of the laterally redistributed organic carbon (Abril et al., 2002).

803      Comparison between the simulation results from ORCHIDEE-$C_{lateral}$ with activated and

804      deactivated erosion and river routing modules indicate that ignoring lateral carbon transport

805      processes in LSM may lead to significant biases in the simulated land carbon budget (Figs. 11

806      and S14). Although the omission of lateral carbon transport in ORCHIDEE-$C_{lateral}$ only resulted

807      in a 1% decrease in simulated average annual total NPP in Europe during 1901-2014 and a 1%

808      increase of annual total Rh, the annual total NBP (=NEP–Rd–DOC and POC to river) is

809 overestimated by 4.5%. Over the same period, the lateral carbon transport only induced a 0.09%

810 decrease in the total SOC and DOC stock in Europe (Fig. S15c), but their spatial distribution was

811 significantly altered (Figs. 12e,f). For instance, in some mountainous regions, the soil erosion

812 induced a reduction of the SOC stock by more than 8%. On the contrary, the sediment and POC

813 deposition in some floodplains led to an increase in SOC stock by more than 8% (Fig. 12f).
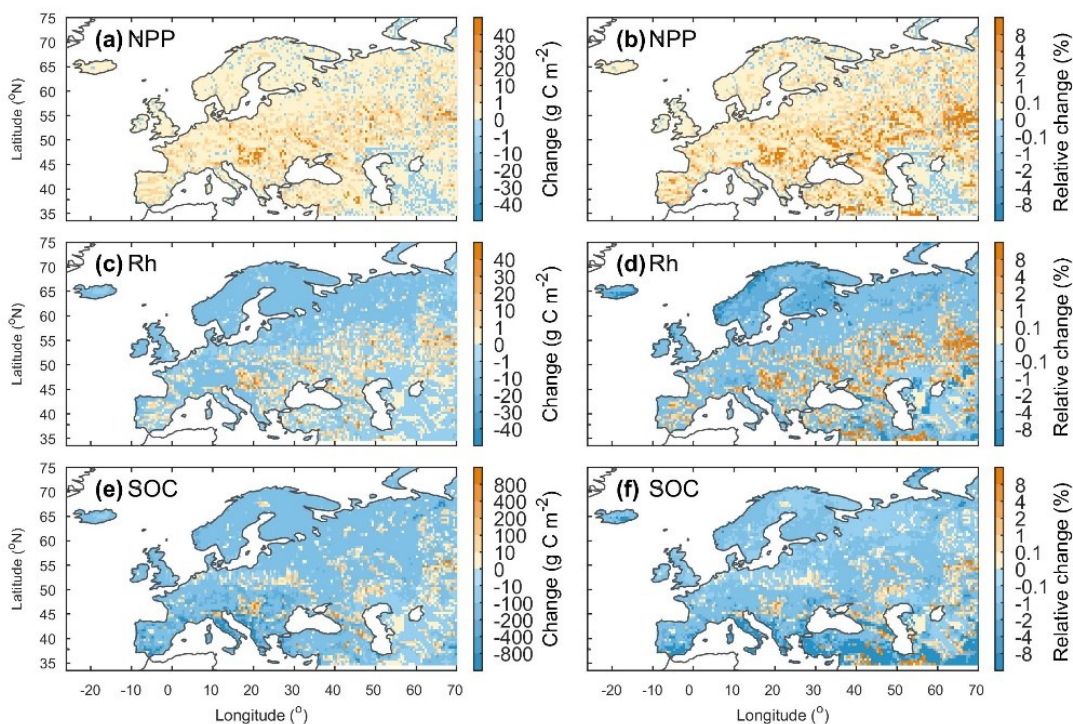
814

815 **Figure 12** Changes (first column) and relative changes (second column) of the net primary

816 production (NPP), heterotrophic respiration (Rh) and total soil organic carbon (SOC, 0-2 m) in

817 Europe due to the lateral carbon transport during 1901-2014. For each variable, the change is

818 calculated as $C_{lat}$ - $C_{nolat}$, where $C_{lat}$ and $C_{nolat}$ are the carbon fluxes or stocks when lateral carbon

819 transport is considered and ignored, respectively. The relative changes is calculated as ($C_{lat}$ -

820 $C_{nolat}$) / $C_{nolat}$ × 100%.

821 Consistent with previous studies (Stallard, 1998; Smith et al., 2001; Hoffmann et al., 2013), our

822 simulation results reveal the importance of sediment deposition in floodplains for the overall

823 SOC budget. From 1901 to 2014, erosion and leaching over Europe totally induced a loss of 3.03

824 Pg organic carbon (POC+DOC) from uplands to the river network, and only 0.65 Pg of this

825 carbon was redeposited onto the floodplains. The total stock of soil organic carbon in Europe

826 thus should have decreased by 2.38 Pg C. However, due to the decrease in decomposition rate of

827    the buried organic carbon (including in-situ and ex-situ carbon) in floodplain soils, the total stock

828    of soil organic carbon in Europe only decreased by 0.91 Pg C. Floodplains in Europe have totally

829    protected 2.12 (= 3.03 - 0.91) Pg soil organic carbon from been transported to the sea or be

830    released to the atmosphere in forms of $CO_2$. Although the sequestration of organic carbon in

831    floodplains cannot make up all of the soil organic carbon (POC+DOC) loss, the increased

832    organic carbon stock in floodplains (2.12 Pg C) is much higher than the soil POC loss (0.86 Pg

833    C) induced by soil erosion.

834    **3.4 Uncertainties and future work**

835    In the present version of ORCHIDEE-Claemeral, the lateral transfers of sediment and carbon is

836    simulated using a simplified scheme, due to the fragmented nature of large-scale forcing (e.g.

837    geomorphic properties of the river channel) and validation data (e.g. continuous sediment and

838    carbon concentration data in river streams and deposition/erosion rates in river channels). We

839    recognize that this simplification induces significant uncertainties in model outputs, especially

840    regarding changes in lateral sediment and particulate carbon transfers under climate change and

841    direct human perturbations. Several physics-based algorithms have been proposed to accurately

842    calculate the *TC* of stream flows (Arnold et al., 1995; Molinas and Wu, 2001; Nearing et al.,

843    1989). These algorithms mostly require detailed information about the stream power (e.g. flow

844    speed and depth), geomorphic properties of the river channel (e.g. slope and hydraulic radius)

845    and the physical properties of the sediment particles (e.g. median grain size) (Neitsch et al.,

846    2011). They are good predictors to estimate *TC* in rivers with detailed observation data on local

847    stream, soil, geomorphic properties. Unfortunately, it is not practical to implement those

848    algorithms in ORCHIDEE-$C_{lateral}$ due to the lack of appropriate forcing data at large scale as well

849    as the relatively rough representation of stream flow dynamics compared to hydrological models

850    for small basins. For example, runoff and sediment from all headwater basins in one 0.5° grid

851    cell of ORCHIDEE-$C_{lateral}$ are assumed to flow into one single virtual river channel. Although

852    the total river surface area in each grid cell is represented (obtained from forcing file (Table 1),

853    Lauerwald et al., 2015), the length, width and depth of the river channel are unknown.

854    Furthermore, in reality, there can be multiple river channels in the area represented by each grid

855    cell, and these channels might flow to different directions.

856  We also noticed that previous studies have derived empirical functions of upstream drainage area

857  (e.g. Luo et al., 2017) or upstream runoff (e.g. Yamazaki et al., 2011) to calculate the river width

858  and depth, allowing to simulate the water flow in the river channel using physically-based

859  algorithms. Unfortunately, to obtain a good fit of the simulated river discharges against

860  observations, the parameters in the empirical functions for calculating river width and depth

861  generally need to be calibrated separately for each catchment (Luo et al., 2017), an approach that

862  is incompatible with large-scale simulations like those performed here. Without such calibration,

863  the simulated geometrical properties of the river channel and runoff are prone to large

864  uncertainties, thus rendering the simulation of sediment transport at continental or global scale

865  using physically-based algorithms a more challenging task. Given the difficulty to simulate the

866  detailed hydraulic dynamics of the stream flow at large spatial scale, we thus apply a simple

867  approach (Eq. 8) to calculate the sediment transport capacity. Overall, we encourage future

868  studies to produce large-scale databases on the geomorphic properties of global river channels

869  (e.g. river depth and width) and to develop large-scale sediment transport models which can give

870  a capable of producing more realistic and accurate simulations of sediment deposition, re-

871  detachment and transport processes, as well as including the exchanges of water, sediment and

872  carbon between river stream and floodplains.

873  The simulation of the soil DOC dynamics and leaching in our model need to be further improved

874  to better simulate the seasonal variation of riverine DOC and TOC concentrations. The

875  concentration of soil DOC and the DOC decomposition rate during the lateral transport process

876  in the river network are the two key factors controlling DOC concentration in river flow.  As

877  only a small fraction (< 20%) of the riverine DOC is decomposed during lateral transport  (Fig.

878  8), the overestimated (Fig. 6) seasonal amplitude in riverine DOC (and TOC) concentrations is

879  likely caused by the uncertainties in the simulated seasonal dynamics of the leached soil DOC.

880  The current scheme used in our model for simulating soil DOC dynamics has been calibrated

881  against observed DOC concentrations at several sites in Europe (Camino-Serrano et al., 2018).

882  Although the calibrated model can overall capture the average concentrations of soil DOC, it is

883  not able to fully capture the temporal dynamics of DOC concentrations (Camino-Serrano et al.,

884  2018).  Given this, it is necessary to collect additional observation data on the seasonal dynamics

885  of soil DOC concentration to further calibrate the soil DOC model. In addition, averaged over

886  the various DOC and SOC pools we distinguish in the soils, DOC represents a much more

887  reactive fraction of soil carbon (with a turnover time of several days to a few months) than SOC

888  (with a turnover time of decades to thousands of years). Therefore, soil DOC concentrations

889  experience large seasonal variations, while SOC concentrations generally are much more stable

890  and show very limited seasonal dynamics. Overall, seasonal variations in riverine POC

891  concentrations are mainly controlled by the seasonal dynamics of soil erosion rates, rather than

892  by the seasonal SOC dynamics, which explains a partial decoupling in the behavior of POC

893  compared to that of DOC.

894  Although most processes related to lateral carbon transport have been represented in

895  ORCHIDEE-C$_{lateral}$, there are still omitted processes and large uncertainties in our model. For

896  example, many studies suggest that a substantial portion of the eroded sediment and carbon is

897  deposited downhill at adjacent lowlands as colluviums, rather than exported to the river (Berhe et

898  al., 2007; Smith et al., 2001; Hoffmann et al., 2013; Wang et al., 2010). As the deposition of

899  sediment and carbon within headwater basins can also significantly alter the vertical SOC profile

900  and soil micro-environments (e.g. soil moisture, aeration and density) (Doetterl et al., 2016;

901  Gregorich et al., 1998; Wang et al., 2015; Zhang et al., 2016), omission of this process may

902  result in uncertainties in the simulated vegetation production and SOC decomposition. In

903  addition, the impact of artificial dams and reservoirs on riverine sediment and carbon fluxes is

904  also not represented in our model. Construction of dams generally leads to increased water

905  residence time, nutrient retention, and sediment and carbon trapping in the impounded reservoir

906  (Habersack et al., 2016; Maavara et al., 2017), and can also affect the downstream flooding

907  regime and frequency (Mei et al., 2016; Timpe and Kaplan, 2017). Estimation by Maavara et al.

908  (2017) suggests that the organic carbon trapped or mineralized in global artificial reservoirs is

909  about 13% of the total organic carbon carried by global rivers to the oceans. To more accurately

910  simulate the lateral carbon transport, we plan to include the soil and carbon redistribution within

911  headwater basins and the effects of dams and reservoirs on riverine sediment and carbon fluxes

912  into our model in the near future.

913  The effects of lateral redistribution of water and sediment on vegetation productivity has not

914  been fully represented in our model. As shown above, our model is able to represent the impacts

915  of lateral water redistribution on vegetation productivity though modifying local soil wetness

916  (Figs. 12 and S16). However, in addition to modifying soil wetness, many studies have indicated

917   that the soil erosion and sediment deposition can affect vegetation productivity by modifying soil

918   nutrient (e.g. nitrogen (N) and phosphorus (P)) availability (Bakker et al., 2004; Borrelli et al.,

919   2018; Quine, 2002; Quinton et al., 2010). Recently, terrestrial N and P cycles have already been

920   incorporated into another branch of ORCHIDEE (i.e. the ORCHIDEE-CNP developed by Goll et

921   al., 2017). By coupling our new branch and ORCHIDEE-CNP, it will be possible to develop a

922   more comprehensive LSM that can also simulate the effects of lateral N and P redistribution on

923   vegetation productivity.

924   Although soils are the major source of riverine organic carbon, domestic, agricultural and

925   industrial wastes, as well as river-borne phytoplankton can also make significant contributions

926   (Abril et al., 2002; Meybeck, 1993; Hoffmann et al., 2020). Moreover, previous studies have

927   shown that sewage generally contains highly labile POC while most of the aquatic production is

928   generally mineralized within a short time (Abril et al., 2002; Caffrey et al., 1998). Omission of

929   organic carbon inputs from manure and sewage could potentially lead to an underestimation of

930   $CO_2$ evasion from the European river network. Inclusion of these additional carbon sources

931   should thus help improve simulation of aquatic $CO_2$ evasion.

932   Uncertainties in our simulation results also stem from the forcing data (Table 1) applied in our

933   model. The routing scheme of water, sediment and carbon is driven by a map of stream flow

934   direction at 0.5° spatial resolution (Guimberteau et al., 2012). Comparison between this flow

935   direction map and the flow direction map derived based on high resolution (3″) DEM show

936   discrepancies between the two river flow networks (Fig. S6). As the flow direction directly

937   determines the area of each catchment and the route of river flows, errors in forcing data of flow

938   direction may thus induce uncertainties in the simulated riverine water, sediment and carbon

939   discharges. Land-cover maps are another source of uncertainty. For instance, croplands generally

940   experience significantly larger soil erosion rates than grasslands and forests (Borrelli et al., 2017;

941   Nunes et al., 2011; Zhang et al., 2020). However, croplands in ORCHIDEE are only represented

942   in a simplified way by segmenting them into C3 and C4 crops based on their photosynthesis

943   characteristics. Therefore, our simulations based on land cover data with only two broad groups

944   of crop might not be able to fully capture the seasonal dynamics of planting, canopy growth rate

945   and harvesting for all crop types. Furthermore, the effects of soil conservation practices, which

946   would decrease erosion rates, are ignored in our model. Panagos et al. (2015) have shown that

947 contour farming, stone wall and grass margin techniques have been applied in Europe reduce the

948 risk of soil erosion. However, these soil conservation practices only reduce the average erosion

949 rate in European Union by 3%. Excluding soil conservation practices thus should have limited

950 impact in our simulation results.

951 Further model calibration, evaluation and development is necessary for improving our model.

952 Due to the limitation of observation data, we calibrated the parameters controlling sediment

953 transport, deposition and re-detachment (i.e. $\omega$, $c_{rivdep}$, $c_{flddep}$, $c_{ebed}$ and $c_{ebank}$ in Table S1) in

954 stream and flooding reservoirs only against the observed sediment yield. Even though our model

955 can overall capture the lateral transfers of sediment and carbon in many rivers in central and

956 northern Europe, more observation data are crucially needed to further evaluate the performance

957 of our model, in particular in southern Europe. In addition, it is still unknown whether our model

958 can satisfactorily simulate intermediate processes such as sediment deposition in river channels

959 and floodplains, as well as the rate of river channel erosion. It is also unknown whether our

960 model would perform satisfactorily in regions with very different climates than Europe such as

961 the tropical region. Thus, in the future, an important aim will be to further calibrate our model

962 against more detailed observation data (e.g. sediment deposition rate in river channels and

963 floodplains) and extend the model application to regions of contrasting climate, vegetation and

964 topography. Moreover, the GLORICH database (Hartmann et al., 2019) only provides

965 instantaneous observations of riverine organic carbon concentrations and it is therefore difficult

966 to evaluate the model's ability to reproduce temporal trends. Therefore, future modelling efforts

967 should be combined with data mining efforts targeting the collection of continuous (e.g. daily)

968 and long-term observational data of organic carbon content and fluxes in streams and rivers.

969

**Conclusions**

971 By merging ORCHILEAK (Lauerwald et al., 2017) and an upgraded version of ORCHIDEE-

972 MUSLE (Zhang et al., 2020) for the simulation of DOC and POC from land to sea, respectively,

973 we developed ORCHIDEE-C$_{lateral}$, a new branch of the ORCHIDEE LSM. ORCHIDEE-C$_{lateral}$

974 simulates the large-scale lateral transport of water, sediment, POC, DOC and $CO_2$ from uplands

975 to the sea through river networks, the deposition of sediment and POC in river channels and

976 floodplains, the decomposition POC and DOC during fluvial transport and the $CO_2$ evasion to

977  the atmosphere, as well as the changes in soil wetness and vertical SOC profiles due to the lateral
978  redistribution of water, sediment and carbon.

979  Evaluation using observation data from European rivers indicate that ORCHIDEE-C$_{lateral}$ can
980  satisfactorily reproduce the observed riverine discharges of water and sediment, bankfull flows
981  and organic carbon concentrations in river flows. Application of ORCHIDEE-C$_{lateral}$ to the entire
982  European river network from 1901 to 2014 reveals that the average annual total carbon delivery
983  to streams and rivers amounts to 47.3±6.6 Tg C yr$^{-1}$, which corresponds to about 4.7% of total
984  NEP and 19.2% of the total NBP of terrestrial ecosystems in Europe. The lateral transfer of
985  water, sediment and carbon can affect the land carbon dynamics through several different
986  mechanisms. Besides directly inducing a spatial redistribution of organic carbon, it can also
987  affect the regional land carbon budget by altering vertical SOC profiles, as well as the soil
988  wetness and soil temperature, which in turn impact vegetation production and the decomposition
989  of soil organic carbon. Overall, omission of lateral carbon transport in ORCHIDEE potentially
990  results in an underestimation of the annual mean NBP in Europe of 4.5%. In regions
991  experiencing high soil erosion or high sediment deposition rate, the lateral carbon transport also
992  changes total SOC stock significantly, by more than 8%.

993  We recognize that ORCHIDEE-C$_{lateral}$ is still entailed with several limitations and significant
994  uncertainties. To address those, we plan to enhance our model with additional processes, such as
995  sediment deposition at downhills or the regulation of lateral transport by dams and reservoirs.
996  We also plan to calibrate and evaluate further our model by extending the observational dataset
997  to regions outside Europe.

998

**Code and data availability**

The source code of ORCHIDEE-Clateral model developed in this study is available online (https://doi.org/10.14768/f2f5df9f-26da-4618-b69c-911f17d7e2ed) from 22 July, 2019. All forcing and validation data used in this study are publicly available online. The specific sources for these data can be found in section Table 1.

**Author contributions**

HZ, RL and PR designed the study. HZ and RL conducted the model development and simulation experiments. PR, KV, PC, VN, BG and WY provided critical contribution to the model development and the design of simulation experiments. HZ conducted the model calibration, validation and the data analysis. RL, PR, PC, KV and BG provided support on collecting forcing and validation data. HZ, RL and PR wrote the manuscript. All authors contributed to interpretation and discussion of results and improved the manuscript.

**Competing interests**

The contact author has declared that neither they nor their co-authors have any competing interests.

**Acknowledgements**

HZ and PR acknowledges the 'Lateral-CNP' project (No. 34823748) supported by the Fonds de la Recherche Scientifique –FNRS and the VERIFY project that received funding from the European Union's Horizon 2020 research and innovation program under grant agreement No. 776810. RL and PC acknowledge funding by the French state aid managed by the ANR under the "Investissements d'avenir" programme [ANR-16-CONV-0003_Cland]. P.R. received funding from the European Union's Horizon 2020 research and innovation programme under Grant Agreement no. 101003536 (ESM2025 – Earth System Models for the Future).

# References:

Abotalib, A. Z., and Mohamed, R. S. A: Surface evidences supporting a probable new concept for the river systems evolution in Egypt: a remote sensing overview. Environ. Earth Sci., 69, 1621-1635, 2012.

Abrams, M., Crippen, R., and Fujisada, H.: ASTER Global Digital Elevation Model (GDEM) and ASTER Global Water Body Dataset (ASTWBD). Remote Sens., 12, 2020.

Abril, G., Nogueira, M., Etcheber, H., Cabecadas, G., Lemaire, E., and Brogueira, M. J.: Behaviour of organic carbon in nine contrasting European estuaries. Estuar., Coast. Shelf Sci., 54, 241-262, 2002.

Arnold, J. G., Williams, J. R., and Maidment, D. R.: Continuous-time water and sediment-routing model for large basins. J. Hydraul. Eng., 121, 171-179, 1995.

Bakker, M. M., Govers, G., and Rounsevell, M. D. A.: The crop productivity–erosion relationship: an analysis based on experimental work. Catena, 57, 55-76, 2004.

Battin, T. J., Luyssaert, S., Kaplan, L. A., Aufdenkampe, A. K., Richter, A., and Tranvik, L. J.: The boundless carbon cycle. Nat. Geosci.e, 2, 598-600, 2009.

Berhe, A. A., Harte, J., Harden, J. W., and Torn, M. S.: The Significance of the Erosion-induced Terrestrial Carbon Sink. BioScience, 57, 337-346, 2007.

Beusen, A. H. W., Dekkers, A. L. M., Bouwman, A. F., Ludwig, W., and Harrison, J.: Estimation of global river transport of sediments and associated particulate C, N, and P. Global Biogeochem. Cycles, 19, https://doi.org/10.1029/2005GB002453, 2005.

Borrelli, P., Robinson, D. A., Fleischer, L. R., Lugato, E., Ballabio, C., Alewell, C., Meusburger, K., Modugno, S., Schütt, B., Ferro, V., Bagarello, V., Oost, K. V., Montanarella, L., and Panagos, P.: An assessment of the global impact of 21st century land use change on soil erosion. Nat. Commun., 8, 2017.

Borrelli, P., Van Oost, K., Meusburger, K., Alewell, C., Lugato, E., and Panagos, P.: A step towards a holistic assessment of soil degradation in Europe: Coupling on-site erosion with sediment transfer and carbon fluxes. Environ. Res., 161, 291-298, 2018.

Caffrey, J. M., Coloern, J. E., and Grenz, C.: Changes in production and respiration during a spring phytoplankton bloom in San Francisco Bay, California, USA: implications for net ecosystem metabolism. Mar. Ecol. Prog. Ser., 172, 1-12, 1998.

Camino-Serrano, M., Guenet, B., Luyssaert, S., Ciais, P., Bastrikov, V., De Vos, B., Gielen, B., Gleixner, G., Jornet-Puig, A., Kaiser, K., Kothawala, D., Lauerwald, R., Peñuelas, J., Schrumpf, M., Vicca, S., Vuichard, N., Walmsley, D., and Janssens, I. A.: ORCHIDEE-SOM: modeling soil organic carbon (SOC) and dissolved organic carbon (DOC) dynamics along vertical soil profiles in Europe. Geosci. Model Dev., 11, 937-957, 2018.

Campoy, A., Ducharne, A., Cheruy, F., Hourdin, F., Polcher, J., and Dupont, J. C.: Response of land surface fluxes and precipitation to different soil bottom hydrological conditions in a general circulation model. J. Geophys. Res.: Atmos., 118, 10,725-710,739, 2013.

Castro, J. M., and Thorne, C. R.: The stream evolution triangle: Integrating geology, hydrology, and biology. River Res. Appl., 35, 315-326, 2019.

Chaplot, V. A. M., Rumpel, C., and Valentin, C.: Water erosion impact on soil and carbon redistributions within

1064    uplands of Mekong River. Global Biogeochem. Cycles, 19, GB4004, 2005.

1065    Chappell, A., Baldock, J., and Sanderman, J.: The global significance of omitting soil erosion from soil organic

1066        carbon cycling schemes. Nat. Clim. Chang., 6, 187-191, 2016.

1067    Chini, L. P., Hurtt, G. C., and Frolking, S.: Harmonized Global Land Use for Years 1500 – 2100, V1. Data set.

1068        Available on-line [http://daac.ornl.gov] from Oak Ridge National Laboratory Distributed Active Archive

1069        Center, Oak Ridge, Tennessee, USA, http://dx.doi.org/10.3334/ORNLDAAC/1248, 2014.

1070    Ciais, P., Sabine, C., Bala, G., Bopp, L., Brovkin, V., Canadell, J., Chhabra, A., DeFries, R., Galloway, J., Heimann,

1071        M., Jones, C., Le Quéré, C., Myneni, R. B., Piao, S. L., and Thornton, P.: Carbon and Other Biogeochemical

1072        Cycles, in: Stocker, T. F., Qin, D., Plattner, G.-K., Tignor, M., Allen, S. K., Boschung, J., Nauels, A., Xia, Y.,

1073        Bex, V., and Midgley, P. M. (Eds.), Climate Change 2013: The Physical Science Basis. Contribution of

1074        Working Group I to the Fifth Assessment Report of the Intergovernmental Panel on Climate Change

1075        Cambridge University Press, Cambridge, United Kingdom and New York, NY, USA, 2013.

1076    Ciais, P., Yao, Y., Gasser, T., Baccini, A., Wang, Y., Lauerwald, R., Peng, S., Bastos, A., Li, W., Raymond, P. A.,

1077        Canadell, J. G., Peters, G. P., Andres, R. J., Chang, J., Yue, C., Dolman, A. J., Haverd, V., Hartmann, J.,

1078        Laruelle, G., Konings, A. G., King, A. W., Liu, Y., Luyssaert, S., Maignan, F., Patra, P. K., Peregon, A.,

1079        Regnier, P., Pongratz, J., Poulter, B., Shvidenko, A., Valentini, R., Wang, R., Broquet, G., Yin, Y.,

1080        Zscheischler, J., Guenet, B., Goll, D. S., Ballantyne, A. P., Yang, H., Qiu, C., and Zhu, D.: Empirical estimates

1081        of regional carbon budgets imply reduced global soil heterotrophic respiration. Natl. Sci. Rev., 8,

1082        https://doi.org/10.1093/nsr/nwaa145, 2021.

1083    Cohen, S., Kettner, A. J., and Syvitski, J. P. M.: Global suspended sediment and water discharge dynamics between

1084        1960 and 2010: Continental trends and intra-basin sensitivity. Glob. Planet. Change, 115, 44-58, 2014.

1085    Cole, J. J., Prairie, Y. T., Caraco, N. F., McDowell, W. H., Tranvik, L. J., Striegl, R. G., Duarte, C. M., Kortelainen,

1086        P., Downing, J. A., Middelburg, J. J., and Melack, J.: Plumbing the Global Carbon Cycle: Integrating Inland

1087        Waters into the Terrestrial Carbon Budget. Ecosystems, 10, 172-185, 2007.

1088    Coulthard, T. J., and Van de Wiel, M. J.: Modelling river history and evolution. Philosophical Transactions A

1089        Mathematical, Phys. Eng. Sci., 370, 2123-2142, 2012.

1090    d'Orgeval, T., Polcher, J., and de Rosnay, P.: Sensitivity of the West African hydrological cycle in ORCHIDEE to

1091        infiltration processes, Hydrol. Earth Syst. Sci., 12, 1387–1401, https://doi.org/10.5194/hess-12-1387-2008,

1092        2008.

1093    Dirmeyerm, P. A., Gao, X., Zhao, M., Guo, Z., Oki, T., and Hanasaki, N.: GSWP-2: Multimodel Analysis and

1094        Implications for Our Perception of the Land Surface. Bull. Amer. Meteorol. Soc., 87, 1381-1398, 2006.

1095    Doetterl, S., Berhe, A. A., Nadeu, E., Wang, Z., Sommer, M., and Fiener, P.: Erosion, deposition and soil carbon: A

1096        review of process-level controls, experimental tools and models to address C cycling in dynamic landscapes.

1097        Earth Sci. Rev., 154, 102-122, 2016.

1098    Drake, T. W., Raymond, P. A., and Spencer, R. G. M.: Terrestrial carbon inputs to inland waters: A current

1099        synthesis of estimates and uncertainty. Limn.Oceanogr. Lett., 3, 132-142, 2018.

1100    FAO/IIASA/ISRIC/ISSCAS/JRC: Harmonized World Soil Database (version 1.2), FAO, Rome, Italy and IIASA,

Laxenburg, Austria, 2012.

Galy, V., France-Lanord, C., and Lartiges, B.: Loading and fate of particulate organic carbon from the Himalaya to the Ganga–Brahmaputra delta. Geochim. Cosmochim. Acta, 72, 1767-1787, 2008.

Gassman, P. W., Sadeghi, A. M., and Srinivasan, R.: Applications of the SWAT Model Special Section: Overview and Insights. J. Environ. Qual., 43, 1-8, 2014.

Gregorich, E. G., Greer, K. J., Anderson, D. W., and Liang, B. C.: Carbon distribution and losses: erosion and deposition effects. Soil Tillage Res., 47, 291-302, 1998.

Guenet, B., Camino-Serrano, M., Ciais, P., Tifafi, M., Maignan, F., Soong, J. L., and Janssens, I. A.: Impact of priming on global soil carbon stocks. Glob. Change Biol., 24, 1873-1883, 2018.

Guenet, B., Moyano, F. E., Peylin, P., Ciais, P., and Janssens, I. A.: (2016) Towards a representation of priming on soil carbon decomposition in the global land biosphere model ORCHIDEE (version 1.9.5.2). Geosci. Model Dev., 9, 841-855, 2016.

Guenet, B., Neill, C., Bardoux, G., and Abbadie, L.: Is there a linear relationship between priming effect intensity and the amount of organic matter input? Appl. Soil Ecol., 46, 436-442, 2010.

Guimberteau, M., Drapeau, G., Ronchail, J., Sultan, B., Polcher, J., Martinez, J. M., Prigent, C., Guyot, J. L., Cochonneau, G., Espinoza, J. C., Filizola, N., Fraizy, P., Lavado, W., De Oliveira, E., Pombosa, R., Noriega, L., and Vauchel, P.: Discharge simulation in the sub-basins of the Amazon using ORCHIDEE forced by new datasets. Hydrol. Earth Syst. Sci., 16, 911-935, 2012.

Guimberteau, M., Zhu, D., Maignan, F., Huang, Y., Yue, C., Dantec-Nédélec, S., Ottlé, C., Jornet-Puig, A., Bastos, A., Laurent, P., Goll, D., Bowring, S., Chang, J., Guenet, B., Tifafi, M., Peng, S., Krinner, G., Ducharne, A., Wang, F., Wang, T., Wang, X., Wang, Y., Yin, Z., Lauerwald, R., Joetzjer, E., Qiu, C., Kim, H., and Ciais, P.: ORCHIDEE-MICT (revision 4126), a land surface model for the high-latitudes: model description and validation. Geosci. Model Dev., 11, 121-163, 2018.

Habersack, H., Hein, T., Stanica, A., Liska, I., Mair, R., Jager, E., Hauer, C. and Bradley, C.: Challenges of river basin management: Current status of, and prospects for, the River Danube from a river engineering perspective. Sci. Total Environ., 543, 828-845, 2016.

Hanson, P. C., Hamilton, D. P., Stanley, E. H., Preston, N., Langman, O. C., and Kara, E. L.: Fate of allochthonous dissolved organic carbon in lakes: a quantitative approach. PLoS One, 6, e21884, 2011.

Haregeweyn, N., Poesen, J., Deckers, J., Nyssen, J., Haile, M., Govers, G., Verstraeten, G., and Moeyersons, J.: Sediment-bound nutrient export from micro-dam catchments in Northern Ethiopia. Land Degrad. Dev., 19, 136-152, 2008.

Hartmann, J., Lauerwald, R., and Moosdorf, N.: GLORICH - Global river chemistry database, in: PANGAEA (Ed.), 2019.

Hengl, T., de Jesus, J. M., MacMillan, R. A., Batjes, N. H., Heuvelink, G. B., Ribeiro, E., Samuel-Rosa, A., Kempen, B., Leenaars, J. G., Walsh, M. G., and Gonzalez, M. R.: SoilGrids1km--global soil information based on automated mapping. PLoS One, 9, e105992, 2014.

Hu, Y., Kuhn, N. J.: Erosion-induced exposure of SOC to mineralization in aggregated sediment. Catena, 137, 517-

525, 2016.

Hoffmann, T. O.: 9.20 - Carbon Sequestration on Floodplains, in: Treatise on Geomorphology (Second Edition), edited by: Shroder, J. F., Academic Press, Cambridge, Massachusetts, United States, 10, 458-477, 2022, https://doi.org/10.1016/B978-0-12-818234-5.00069-9.

Hoffmann, T. O., Baulig, Y., Fischer, H., and Blöthe, J.: Scale breaks of suspended sediment rating in large rivers in Germany induced by organic matter. Earth Surf. Dynam., 8, 661–678, 2020.

Hoffmann, T., Schlummer, M., Notebaert B., Verstraeten, G., and Korup, O.: Carbon burial in soil sediments from Holocene agricultural erosion,Central Europe. Glob. Biogeochem. Cy., 27, 828-835, 2013.

Janssens, I. A., Freibauer, A., Ciais, P., Smith, P., Nabuurs, G. J., Folberth, G., Schlamadinger, B., Hutjes, R. W., Ceulemans, R., Schulze, E. D., Valentini, R., and Dolman, A. J.: Europe's terrestrial biosphere absorbs 7 to 12% of European anthropogenic CO2 emissions. Science, 300, 1538-1542, 2003.

Jetten, V., Govers, G., Hessel, R.: Erosion models: quality of spatial predictions. Hydrol. Process., 17, 887-900, 2003.

Kalbitz, K., Schmerwitz, J., Schwesig, D., and Matzner, E.: Biodegradation of soil-derived dissolved organic matter as related to its properties. Geoderma, 113, 273-291, 2003.

Knapp, A. K., Briggs, J. M., and Koelliker, J. K.: Frequency and Extent of Water Limitation to Primary Production in a Mesic Temperate Grassland. Ecosystems, 4, 19-28, 2001.

Krinner, G., Viovy, N., de Noblet-Ducoudré, N., Ogée, J., Polcher, J., Friedlingstein, P., Ciais, P., Sitch, S., and Prentice, I. C.: A dynamic global vegetation model for studies of the coupled atmosphere-biosphere system. Global Biogeochem. Cycles, 19, 2005.

Lal, R.: Soil erosion and the global carbon budget. Environ. Int., 29, 437-450, 2003.

Lal, R.: Soil carbon sequestration impacts on global climate change and food security. Science, 304, 1623-1627, 2004.

Lauerwald, R., Laruelle, G., Hartmann, J., Ciais, P., and Regnier, P.: Spatial patterns in $CO_2$ evasion from the global river network: Spatial patter of riverine pCO2 and FCO2. Global Biogeochem. Cycles, 29, 2015.

Lauerwald, R., Regnier, P., Camino-Serrano, M., Guenet, B., Guimberteau, M., Ducharne, A., Polcher, J., and Ciais, P.: ORCHILEAK (revision 3875): a new model branch to simulate carbon transfers along the terrestrial–aquatic continuum of the Amazon basin. Geosci. Model Dev., 10, 3821-3859, 2017.

Lauerwald, R., Regnier, P., Guenet, B., Friedlingstein, P., and Ciais, P.: How Simulations of the Land Carbon Sink Are Biased by Ignoring Fluvial Carbon Transfers: A Case Study for the Amazon Basin. One Earth, 3, 226-236, 2020.

Lehner, B., Verdin, K., and Jarvis, A.: New global hydrography derived from spaceborne elevation data. Eos, Transactions, AGU, 89, 93-94, 2008.

Lugato, E., Paustian, K., Panagos, P., Jones, A., and Borrelli, P.: Quantifying the erosion effect on current carbon budget of European agricultural soils at high spatial resolution. Glob. Change Biol., 22, 1976-1984, 2016.

Luo, X., Li, H., Leung L.R., Tesfa, T. K., Getirana, A., Papa, F., and Hess L. L.: Modeling surface water dynamics in the Amazon Basin using MOSART-Inundation v1.0: impacts of geomorphological parameters and river flow

1175    representation. Geosci. Model Dev., 10, 1233-1259, 2017.

1176    Maavara, T., Lauerwald, R., Regnier, P., and Van Cappellen, P.: Global perturbation of organic carbon cycling by
1177        river damming. Nat. Commun., 8, 15347, 2017.

1178    Mei, X., Van Gelder, P., Dai, Z., and Tang, Z.: Impact of dams on flood occurrence of selected rivers in the United
1179        States. Front. Earth Sci., 11, 268-282, 2016.

1180    Meybeck, M.: Riverine transport of atmospheric carbon: sources, global typology and budget. Water Air Soil
1181        Pollut., 70, 443-463, 1993.

1182    Molinas, A., and Wu, B.: Transport of sediment in large sand-bed rivers. J. Hydraul. Res., 39, 135-146, 2001.

1183    Moore, I. D., and Wilson, J. P.: Length-slope factors for the Revised Universal Soil Loss Equation: Simplified
1184        method of estimation. J. Soil Water Conserv., 47, 423-428, 1992.

1185    Nadeu, E., de Vente, J., Martínez-Mena, M., and Boix-Fayos, C.: Exploring particle size distribution and organic
1186        carbon pools mobilized by different erosion processes at the catchment scale. J. Soils Sediments, 11, 667-678,
1187        2011.

1188    Naipal, V., Lauerwald, R., Ciais, P., Guenet, B., and Wang, Y.: CE-DYNAM (v1): a spatially explicit process-based
1189        carbon erosion scheme for use in Earth system models. Geosci. Model Dev., 13, 1201-1222, 2020.

1190    Nakhavali, M., Lauerwald, R., Regnier, P., Guenet, B., Chadburn, S., and Friedlingstein, P.: Leaching of dissolved
1191        organic carbon from mineral soils plays a significant role in the terrestrial carbon balance. Glob. Change Biol.,
1192        27, 1083-1096, 2021.

1193    Nardi, F., Annis, A., Di Baldassarre, G., Vivoni, E.R., and Grimaldi, S.: GFPLAIN250m, a global high-resolution
1194        dataset of Earth's floodplains. Sci. Data, 6, 180309, 2019.

1195    Nearing, M. A., Foster, G. R., Lane, L. J., and Finkner, S. C.: A Process-Based Soil Erosion Model for USDA-
1196        Water Erosion Prediction Project Technology. Transactions of the Asae, 32, 1587-1593, 1989.

1197    Neckles, H. A, and Neill, C.: Hydrologic control of litter decomposition in seasonally flooded prairie marshes.
1198        Hydrobiologia, 286, 155-165, 1994.

1199    Neitsch, S. L., Williams, J. R., Arnold, J. G., and Kiniry, J. R.: Soil and Water Assessment Tool Theoretical
1200        Documentation Version 2009.  Texas Water Resources Institute, College Station, 2011.

1201    Nie, X., Li, Z., He, J., Huang, J., Zhang, Y., Huang, B., Ma, W., Lu, Y., and Zeng, G.: Enrichment of organic carbon
1202        in sediment under field simulated rainfall experiments. Environ. Earth Sci., 74, 5417-5425, 2015.

1203    Nodvin, S. C., Driscoll, C. T., and Likens, G. E.: Simple partitioning of anions and dissolved organic carbon in a
1204        forest soil. Soil Sci., 142, 27-35, 1986.

1205    Nunes, A. N., de Almeida, A. C., and Coelho, C. O. A.: (2011) Impacts of land use and cover type on runoff and soil
1206        erosion in a marginal area of Portugal. Appl. Geogr., 31, 687-699, 2011.

1207    Oeurng, C., Sauvage, S., and Sánchez-Pérez, J. M.: Assessment of hydrology, sediment and particulate organic
1208        carbon yield in a large agricultural catchment using the SWAT model. J. Hydrol., 401, 145-153, 2011.

1209    Parton, W. J., Schimel, D. S., Cole, C. V., and Ojima, D. S.: Analysis of Factors Controlling Soil Organic Matter
1210        Levels in Great Plains Grasslands1. Soil Sci. Soc. Am. J., 51, 1173-1179, 1987.

1211    Parton, W. J., Stewart, J. W. B., and Cole, C. V.: Dynamics of C, N, P and S in grassland soils: a model.

1212       Biogeochemistry, 5, 109-131, 1988.

1213    Polyakov, V. O., and Lal, R.: Soil organic matter and CO 2 emission as affected by water erosion on field runoff

1214       plots. Geoderma, 143, 216-222, 2008.

1215    Quine, T. A.: An investigation of spatial variation in soil erosion, soil properties and crop production with an

1216       agricultural field in Devon, UK. J. Soil Water Conserv., 57, 55-65, 2002.

1217    Quinton, J. N., Govers, G., Van Oost, K., and Bardgett, R. D.: The impact of agricultural soil erosion on

1218       biogeochemical cycling. Nat. Geosci., 3, 311-314, 2010.

1219    Raymond, P. A., Hartmann, J., Lauerwald, R., Sobek, S., McDonald, C., Hoover, M., Butman, D., Striegl, R.,

1220       Mayorga, E., Humborg, C., Kortelainen, P., Durr, H., Meybeck, M., Ciais, P., and Guth, P.: Global carbon

1221       dioxide emissions from inland waters. Nature, 503, 355-359, 2013.

1222    Reddy, K. R., Patrick Jr, and W. H.: Effect of alternate aerobic and anaerobic conditions on redox potential, organic

1223       matter decomposition and nitrogen loss in a flooded soil. Soil Biol. Biochem., 7, 87-94, 1975.

1224    Regnier, P., Friedlingstein, P., Ciais, P., Mackenzie, F. T., Gruber, N., Janssens, I. A., Laruelle, G. G., Lauerwald,

1225       R., Luyssaert, S., Andersson, A. J., Arndt, S., Arnosti, C., Borges, A. V., Dale, A. W., Gallego-Sala, A.,

1226       Goddéris, Y., Goossens, N., Hartmann, J., Heinze, C., Ilyina, T., Joos, F., LaRowe, D. E., Leifeld, J., Meysman,

1227       F. J. R., Munhoven, G., Raymond, P. A., Spahni, R., Suntharalingam, P., and Thullner, M.: Anthropogenic

1228       perturbation of the carbon fluxes from land to ocean. Nat. Geosci., 6, 597-607, 2013.

1229    Regnier, P., Resplandy, L., Najjar, R. G., and Ciais, P.: The land-toocean loops for the global carbon cycle. Nature,

1230       603, 401-410, 2022.

1231    Reynolds, C., Jackson, T., and Rawls, W.: Estimating available water content by linking the FAO soil map of the

1232       world with global soil profile databases and pedo-transfer functions, Am. Geophys. Union Fall Meet. EOS

1233       Trans. Spring Meet. Suppl., 80, S132, 1999.

1234    Sanderman, J., Hengl, T., and Fiske, G. J.: Soil carbon debt of 12,000 years of human land use. Proc. Natl. Acad.

1235       Sci., 114, 9575-9580, 2017.

1236    Schneider, C., Flörke, M., Eisner, E., and Voss, F.: Large scale modelling of bankfull flow: An example for Europe.

1237       J. Hydrol., 408, 235-245, 2011.

1238    Shangguan, W., Dai, Y., Duan, Q., Liu, B., and Yuan, H.: A global soil data set for earth system modeling. J. Adv.

1239       Model. Earth Syst., 6, 249-263, 2014.

1240    Sharpley, A. N., and Williams, J. R.: EPIC-erosion/productivity impact calculator: 2. User manual. Technical

1241       Bulletin - United States Department of Agriculture, 4, 206-207, 1990.

1242    Smith, S. V., Renwick, W. H., Buddemeier, R. W., and Crossland, C.J.: Budgets of soil erosion and deposition for

1243       sediments and sedimentary organic carbon across the conterminous United States. Global Biogeochem. Cycles,

1244       15, 697-707, 2001.

1245    Stallard, R. F.: Terrestrial sedimentation and the carbon cycle: Coupling weathering and erosion to carbon burial.

1246       Global Biogeochem. Cycles, 12, 231-257, 1998.

1247    Stocker, B. D., Zscheischler, J., Keenan, T. F., Prentice, I. C., Seneviratne, S. I., and Peñuelas, J.: Drought impacts

1248       on terrestrial primary production underestimated by satellite monitoring. Nat. Geosci., 12, 264-270, 2019.

1249 Telmer, K., and Veizer, J.: Carbon fluxes,pCO   and substrate weathering in a large northern2river basin, Canada:

1250    carbon isotope perspectives. Chem. Geol., 159, 61-86, 1999.

1251 Tian, H., Yang, Q., Najjar, R. G., Ren, W., Friedrichs, M. A. M., Hopkinson, C. S., and Pan, S.: Anthropogenic and

1252    climatic influences on carbon fluxes from eastern North America to the Atlantic Ocean: A process-based

1253    modeling study. J. Geophys. Res.: Biogeosci., 120, 757-772, 2015.

1254 Timpe, K., and Kaplan, D.: The changing hydrology of a dammed Amazon. Sci. Adv., 3, 11, e1700611, 2017.

1255 Van Hemelryck, H., Govers, G., Van Oost, K., and Merckx, R.: Evaluating the impact of soil redistribution on the in

1256    situ mineralization of soil organic carbon. Earth Surf. Process. Landf., 36, 427-438, 2011.

1257 Van Oost, K., Quine, T. A., Govers, G., De Gryze, S., Six, J., Harden, J. W., Ritchie, J. C., McCarty, G. W.,

1258    Heckrath, G., Kosmas, C., Giraldez, J. V., da Silva, J. R., and Merckx, R.: The impact of agricultural soil

1259    erosion on the global carbon cycle. Science, 318, 626-629, 2007.

1260 Vigiak, O., Malago, A., Bouraoui, F., Vanmaercke, M., Obreja, F., Poesen, J., Habersack, H., Feher, J., and Groselj,

1261    S.: Modelling sediment fluxes in the Danube River Basin with SWAT. Sci. Total Environ., 599-600, 992-1012,

1262    2017.

1263 Vörösmarty, C. J., Fekete, B. M., Meybeck, M., and Lammers, R. B.: Geomorphometric attributesof the global

1264    system of rivers at 30-minute spatial resolution. J. Hydrol., 237, 17-39, 2000.

1265 Wang, X., Cammeraat, E. L., Romeijn, P., and Kalbitz, K.: Soil organic carbon redistribution by water erosion--the

1266    role of CO2 emissions for the carbon budget. PLoS One, 9, e96299, 2014a.

1267 Wang, Z., Govers, G., Steegen, A., Clymans, W., Van den Putte, A., Langhans, C., Merckx, R., and Van Oost, K.:

1268    Catchment-scale carbon redistribution and delivery by water erosion in an intensively cultivated area.

1269    Geomorphology, 124, 65-74, 2010.

1270 Wang, Z., Hoffmann, T., Six, J., Kaplan, J. O., Govers, G., Doetterl, S., and Van Oost, K.: Human-induced erosion

1271    has offset one-third of carbon emissions from land cover change. Nat. Clim. Chang., 7, 345-349, 2017.

1272 Wang, Z., Van Oost, K., and Govers, G.: Predicting the long-term fate of buried organic carbon in colluvial soils.

1273    Global Biogeochem. Cycles, 29, 65-79, 2015.

1274 Wang, Z., Van Oost, K., Lang, A., Quine, T., Clymans, W., Merckx, R., Notebaert, B., and Govers, G.: The fate of

1275    buried organic carbon in colluvial soils: a long-term perspective. Biogeosciences, 11, 873-883, 2014b.

1276 Xu, X., Sherry, R. A., Niu, S., Li, D., and Luo, Y.: Net primary productivity and rain-use efficiency as affected by

1277    warming, altered precipitation, and clipping in a mixed-grass prairie. Glob. Change Biol., 19, 2753-2764, 2013.

1278 Yamazaki, D., Kanae, S., Kim, H., and Oki T.: A physically based description of floodplain inundation dynamics in

1279    a global river routing model. Water Resour. Res., 47, W04501, doi:10.1029/2010WR009726, 2011.

1280 Zhang, H., Lauerwald, R., Regnier, P., Ciais, P., Yuan, W., Naipal, V., Guenet, B., Van Oost, K., and Camino-

1281    Serrano, M.: Simulating Erosion-Induced Soil and Carbon Delivery From Uplands to Rivers in a Global Land

1282    Surface Model. J. Adv. Model. Earth Syst., 12, e2020MS002121, 2020.

1283 Zhang, H., Liu, S., Yuan, W., Dong, W., Xia, J., Cao, Y., and Jia, Y.: Loess Plateau check dams can potentially

1284    sequester eroded soil organic carbon. J. Geophys. Res. Biogeosci., 121, 2016.

1285 Zhang, H., Liu, S., Yuan, W., Dong, W., Ye, A., Xie, X., Chen, Y., Liu, D., Cai, W., and Mao, Y.: Inclusion of soil

1286    carbon lateral movement alters terrestrial carbon budget in China. Sci. Rep., 4, 7247, 2014.